

# Constraints on New Physics with Light Mediators and Generalized Neutrino Interactions via Coherent Elastic Neutrino Nucleus Scattering

S. Karadağ,<sup>1,2,\*</sup> M. Deniz,<sup>3,†</sup> S. Karmakar,<sup>2,4</sup> M. K. Singh,<sup>2,5</sup> M. Demirci,<sup>6</sup> Greeshma C.,<sup>2,7</sup> H. B. Li,<sup>2</sup> S. T. Lin,<sup>8</sup> M. F. Mustamin,<sup>6</sup> V. Sharma,<sup>9</sup> L. Singh,<sup>7</sup> M. K. Singh,<sup>4</sup> V. Singh,<sup>7</sup> and H. T. Wong<sup>2</sup>  
(The TEXONO Collaboration)

<sup>1</sup>*Department of Physics Engineering, Istanbul Technical University, Sarıyer, İstanbul TR34467, Türkiye*

<sup>2</sup>*Institute of Physics, Academia Sinica, Taipei 11529*

<sup>3</sup>*Department of Physics, Dokuz Eylül University, Buca, İzmir TR35160, Türkiye*

<sup>4</sup>*Department of Physics, Institute of Applied Sciences and Humanities, GLA University, Mathura 281406, India*

<sup>5</sup>*Department of Physics, Institute of Science, Banaras Hindu University, Varanasi 221005, India*

<sup>6</sup>*Department of Physics, Karadeniz Technical University, TR61080 Trabzon, Türkiye*

<sup>7</sup>*Department of Physics, School of Physical and Chemical Sciences, Central University of South Bihar, Gaya 824236, India*

<sup>8</sup>*College of Physics, Sichuan University, Chengdu 610065*

<sup>9</sup>*Department of Physics, H.N.B. Garhwal University, Srinagar 246174, India*

(Dated: May 28, 2025)

We investigate new physics effects on Coherent Elastic Neutrino Nucleus Scattering (CE $\nu$ NS) within the framework of Non-Standard Interactions (NSI) and generalized neutrino interactions (GNI). Additionally, we examine the possibility of light mediators from a simplified model that includes all possible Lorentz-invariant interactions of vector (V), axialvector (A), scalar (S), pseudoscalar (P), and tensor (T) types. Constraints and allowed regions at the 90% C. L. for masses and couplings in each new physics scenario have been obtained through the analysis of TEXONO data, which includes two datasets from a high-purity  $n$ -type point contact (nPC) germanium (Ge) detector (2016) and an advanced  $p$ -type point contact (pPC) Ge detector (2025). The results are presented in comparison with other reactor and accelerator-based neutrino experiments for complementarity.

## I. INTRODUCTION

The interactions of neutrinos with matter [1] have long been considered promising avenues for revealing new physical phenomena. Neutrino-nucleus elastic scattering process [2, 3],

$$\nu_\alpha(\bar{\nu}_\alpha) + N(\mathcal{Z}, \mathcal{N}) \longrightarrow \nu_\alpha(\bar{\nu}_\alpha) + N(\mathcal{Z}, \mathcal{N}), \quad (1.1)$$

where  $\alpha$  stands for lepton flavor ( $e$ ,  $\mu$  or  $\tau$ ) for incoming or outgoing neutrinos and  $N(\mathcal{Z}, \mathcal{N})$  denotes the atomic nucleus, characterized by its atomic number ( $\mathcal{Z}$ ) and neutron number ( $\mathcal{N}$ ). This process is also referred to as Coherent Elastic Neutrino-Nucleus Scattering (CE $\nu$ NS) and serves as an important channel for testing the Standard Model (SM) of electroweak theory, especially in the low energy regime.

### A. Coherent Elastic Neutrino-Nucleus Scattering (CE $\nu$ NS)

CE $\nu$ NS, which involves neutral current (NC) interactions between neutrinos and quarks in an atomic nucleus, is essentially a tree-level process defined within the SM.

However, radiative corrections such as those resulting from loop diagrams also contribute to this interaction and must also be taken into account in precise calculations [4]. In this process, neutrinos interact coherently with a nucleus, whether protons or neutrons, via neutral boson exchange at low energies. Coherent means that neutrinos can reach the interior of the nucleus without breaking it, i.e. the interaction occurs with the nucleus as a whole. Therefore, the wavelength of the process is larger than the nuclear radius and results in a momentum exchange on the order of a few hundred MeV. This means that the complexity of the strong interaction can be encapsulated in a nuclear form factor. The process yields the largest cross-section compared to other neutrino interactions in the low energy regime so far. The cross-section depends on the number of nucleons involved. In particular, the observed cross-section increases with the square of the number of neutrons, since the weak mixing angle affects and limits the contribution from proton interactions. However, this process is difficult to detect because the nuclear recoil energy is limited to the low keV scale. This criterion is necessary to ensure that the nucleus interacts coherently with the neutrino. This challenging goal was finally achieved in 2017 with the advancement of accelerator neutrino technology by the COHERENT Collaboration [5, 6], several decades after its initial formulation [2].

Since the first detection of CE $\nu$ NS, numerous efforts have been made to better understand the phenomena. The COHERENT Collaboration updated their experiment using liquid Argon (LAr) [7]. They also announced

\* Corresponding Author: karadags@itu.edu.tr

† Corresponding Author: muhammed.deniz@deu.edu.tr

the first detection of  $\text{CE}\nu\text{NS}$  with pPC Ge detector, reinforcing the importance of Ge detectors in precision studies of low-energy neutrino interactions [8] and plan to further upgrade their experimental facilities by adapting liquid Xenon detector as a target [9]. The CENNS team at Fermilab also aims to detect the  $\text{CE}\nu\text{NS}$  process using the Booster Neutrino Beam at the facility [10]. Furthermore, reactor neutrino experiments are also contributing to the detection of the process in order to achieve lower nuclear threshold energy. The CONUS Collaboration provided strong limits [11] with Ge detectors at the Brokdorf Nuclear Power Plant in Germany. The follow-up CONUS+ project recently reported preliminary results [12] on a positive observation of  $\text{CE}\nu\text{NS}$  at a significance of  $3.7\sigma$  at the Leibstadt nuclear power plant (KKL) in Switzerland, marking a significant step in reactor neutrino  $\text{CE}\nu\text{NS}$  searches. Alongside CONUS, other reactor-based efforts include TEXONO [13] with a Ge detector located at the Kuo-Sheng Nuclear Power Plant in Taiwan; CONNIE [14] with a CCD detector array at the Angra Power Plant in Rio de Janeiro, Brazil; RICOCHET [15] with both Ge-based and metallic Zn-based smaller detector at the Chooz Nuclear Power Plant in France;  $\nu\text{GeN}$  [16] with high purity Ge detector at the Kalinin Nuclear Power Plant in Russia; Dresden-II [17] with p-type point contact Ge detector in USA, MINER [18] with low threshold cryogenic germanium and silicon detectors at the Nuclear Science Center at Texas in USA;  $\nu\text{CLEUS}$  [19] with  $\text{CaWO}_4$  and  $\text{Al}_2\text{O}_3$  calorimeter arrays and several cryogenic veto detectors operated at millikelvin temperatures; the RED-100 [20] with two-phase Xenon emission detector at the Kalinin Nuclear Power Plant.

Nuclear power plant experiments have high potential for observing the  $\text{CE}\nu\text{NS}$  process, as they meet the coherency criteria ( $> 95\%$ ) due to their high rate of low-energy neutrino flux [21]. Dark matter (DM) experiments, such as XENONnT [22], DARWIN [23], LZ [24], and PandaX-4T [25], are also influenced by this channel, as  $\text{CE}\nu\text{NS}$  plays a crucial role in the neutrino-floor phenomenon, providing an unavoidable background for DM experiments. Recently, the PandaX-4T [26] and XENONnT [27] experiments have reported the first measurements of nuclear recoils from solar  $^8\text{B}$  neutrinos via  $\text{CE}\nu\text{NS}$  with the corresponding statistical significance of  $2.64\sigma$  and  $2.73\sigma$ , respectively, representing the first experimental step towards the neutrino fog.

## B. Non-Standard Interactions in $\text{CE}\nu\text{NS}$

The  $\text{CE}\nu\text{NS}$  process opens up numerous opportunities to expand our understanding of physics. For example, it allows the investigation of neutrino and nuclear properties, such as study of the neutrino magnetic moment [28, 29]. Recent research has also explored potential explanations of sterile neutrinos [30]. Additionally, nuclear properties may be examined through this pro-

cess [31].  $\text{CE}\nu\text{NS}$  plays an important role in astrophysical processes [2, 32] and has been proposed for detecting supernova neutrinos [33], providing a compact and transportable neutrino detector for real-time monitoring nuclear reactors [34], and studying neutron density distributions [35]. Moreover, the potential appearance of new fermions linked to neutrino mass and their role in explaining DM has been recently investigated [36]. The study of weakly interacting massive particle (WIMP) [37, 38] as a candidate of DM is also related to  $\text{CE}\nu\text{NS}$ , as both share a similar nuclear recoil energy range in the few keV scale.  $\text{CE}\nu\text{NS}$  events from solar and atmospheric neutrinos represent an irreducible background [39, 40] for future DM direct detection experiments [41, 42]. Additionally, measuring of the  $\text{CE}\nu\text{NS}$  scattering cross-section serves as a sensitive probe for new physics [43–45], potentially enabling the detection of new light bosons [46, 47], which is crucial for advancing our understanding of novel interactions in nature.

Probing NSI through neutrino-nucleus scattering has been a subject of intense interest in recent years [45–55]. These studies have investigated various NSI scenarios, such as those based on simplified models focusing on light mediators [56–68], model-independent approaches effective in the high mediator mass regime [56, 67, 69–74], and exotic neutral current interactions [67, 75–77], along with experimental observables and implications for neutrino flavor physics [51, 78, 79] and astrophysical processes [80–82]. In addition, the studies combining complementary sources such as reactor and accelerator neutrinos [49, 62, 83] have helped to improve sensitivity to multiple interaction types. Collectively, these studies provide a strong foundation for further investigation of a wide range of NSI scenarios and underscore the need for ongoing research using both current and future neutrino experimental data.

## C. Scope and Structure of This Work

In this work, we provide a comprehensive analysis of TEXONO reactor neutrino experiment’s sensitivity to all five possible Lorentz-invariant NSI interaction types, both within a simplified model and model-independent frameworks. We explore a simplified model as an alternative approach to investigating physics beyond the SM (BSM). Specifically, we consider generalized neutrino interactions (GNI) as well as the possibility of light mediators from simplified model, which includes vector (V), axialvector (A), scalar (S), pseudoscalar (P), and tensor (T) types. Each is assumed to involve light mediators that couple to neutrinos and the quark constituents of the nucleus. Notably, recent studies have employed an effective neutrino-quark approximation that includes these interaction types [75]. The connections between this effective approximation and NSI have also been examined [84]. Simplified model provides an alternative framework in particle physics to bridge theoretical pre-

diction with experimental measurements. The experimental parameters considered in this model are limited to cross-sections, new particle masses, and couplings. It is important to emphasize that, unlike comprehensive BSM extensions involving numerous particles and decay chains, this model does not fully represent the complexities of actual physics [85]. Nevertheless, explanatory models remain valuable for consideration, including those that can be embedded within potential SM extensions, either dependently or independently.

In this work, in particular, we present the first NSI analysis based on TEXONO experiments, using both nPC–Ge data [86] and recently released pPC–Ge data [87]. In the TEXONO experiment, which studies neutrino interactions in a reactor environment dominated by low-energy electron antineutrinos, we aimed to provide a systematic assessment of how advances in detector technology have increased sensitivity to NSI parameters. We also intend to highlight the important role of the TEXONO experiment in CE $\nu$ NS studies by comparing our results with the existing bounds from other experiments in the literature, both reactor-based and accelerator-based. To this end in this work, we cover all possible interaction types in both simplified model and model-independent approach, as well as exotic neutral current interactions.

We also note that  $\nu$ -e scattering channel, while also sensitive to NSI effects and widely studied in the literature [88–92], is beyond the scope of this work due to its distinct kinematic features and systematic considerations. A proper treatment of this channel requires a dedicated and comprehensive analysis. Specifically, TEXONO Collaboration has previously investigated new physics BSM with this channel given in Refs. [93–96]. This channel can also be studied specifically for generalized NSI using both TEXONO-CsI(Tl) [97] and TEXONO-Ge[87] data and eventually combined the results with CE $\nu$ NS constraints within a more comprehensive NSI framework. For additional context, we refer readers to Refs.[11, 49, 66, 67, 98, 99], which examine NSI sensitivity through  $\nu$ -e scattering across different experimental settings.

In the following sections, we first provide a brief discussion of the theoretical formulation of CE $\nu$ NS, covering differential cross-sections and the effect of the form factor in Section II. In Subsection II A, we delve into GNI derived from simplified model. The formalism and structure of the model-independent NSI of neutrinos and the exotic neutral current interactions are given in Subsection II B and II C, respectively. The observation of CE $\nu$ NS by analysis of the TEXONO experiment and the calculation of expected event rates based on both SM and BSM NSI theories are discussed in Section III. Our analysis methods and final results are introduced in Section IV, starting from the relevant Lagrangian for the new interactions considered in the model and using  $\chi^2$ -analysis methods. This section also presents our findings, including new constraints on coupling and mass parameter

spaces, as well as on four-Fermi point-like interactions of  $\varepsilon_{\alpha\beta}^{fX}$  parameter-space and exotic neutral-current interactions of  $\xi_X$  parameter-space, along with discussions of potential implications. Finally, we summarize and conclude our work in Section V.

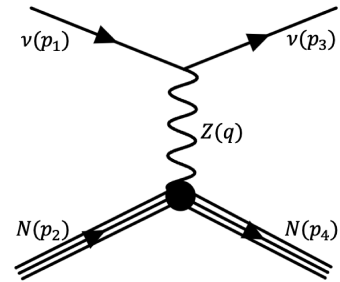


FIG. 1. The Feynman diagram for CE $\nu$ NS process.

## II. FORMALISM

The scattering amplitude for the CE $\nu$ NS process, as shown in Fig. 1, can be expressed as ( $q^2 \ll m_Z^2$ )

$$\mathcal{M} = \frac{G_F}{\sqrt{2}} \bar{\nu}(p_3) \gamma^\mu (1 - \gamma^5) \nu(p_1) \times \bar{N}(p_4) \gamma_\mu (Q_{\text{SM}\nu} - \gamma^5 Q_{\text{SM}A}) N(p_2), \quad (2.1)$$

where  $G_F$  is the Fermi constant. We have used  $G_F/\sqrt{2} = g_W^2/8m_W^2$  and  $m_W = m_Z \cos \theta_W$ , where  $g_W$  and  $m_W$  ( $m_Z$ ) are the weak coupling constant and  $W$  ( $Z$ ) boson mass, respectively.

The SM differential cross-section, incorporating both vector and axialvector weak charge components can be written as:

$$\left[ \frac{d\sigma}{dT_N} \right]_{\text{SM}} = \frac{G_F^2 m_N}{4\pi} (Q_{\text{SM}\nu}^2 \mathcal{K}_V + Q_{\text{SM}A}^2 \mathcal{K}_A), \quad (2.2)$$

where  $m_N$  is the nucleus mass, and the kinetic terms of vector and axialvector,  $\mathcal{K}_V$  and  $\mathcal{K}_A$ , can be described respectively as

$$\begin{aligned} \mathcal{K}_V &= 1 - \frac{m_N T_N}{2E_\nu^2} - \frac{T_N}{E_\nu} + \frac{T_N^2}{2E_\nu^2}, \\ \mathcal{K}_A &= 1 + \frac{m_N T_N}{2E_\nu^2} - \frac{T_N}{E_\nu} + \frac{T_N^2}{2E_\nu^2}. \end{aligned} \quad (2.3)$$

The vector part of the SM weak charge  $Q_{\text{SM}\nu}$  can be written as

$$\begin{aligned} Q_{\text{SM}\nu} &= g_p^V \mathcal{Z} F_Z(q^2) + g_n^V \mathcal{N} F_N(q^2) \\ &= [\mathcal{Z} (1 - 4 \sin^2 \theta_W) - \mathcal{N}] F_V(q^2), \end{aligned} \quad (2.4)$$

where  $\sin^2 \theta_W$  is the weak mixing angle with a value of 0.23867 [1] at  $q^2 \simeq 0$  [4], and  $g_n^V = -1$  and  $g_p^V =$

$1 - 4 \sin^2 \theta_W \simeq 0.0453$  are tree-level vector neutrino-neutron and neutrino-proton couplings, respectively. Including radiative corrections, these couplings are modified to  $g_n^V \simeq -1.0234$  and  $g_p^V(\nu_e) \simeq 0.0762$ , reflecting flavor dependence of proton coupling for electron neutrinos [100]. The cross-section in Eq. (2.2) is enhanced by  $\mathcal{N}^2$  due to the multiplication factor of  $g_p^V$ , making the contribution from the  $Z$  boson relatively small. Despite the smallness of this factor, it remains important because it includes the weak mixing angle,  $\sin^2 \theta_W$ .

Nuclear physics effects in CE $\nu$ NS are incorporated via the weak nuclear form factors  $F_{\mathcal{N}}$  for neutrons and  $F_Z$  for protons given in Eq. (2.4). In this work, these are assumed to be equal such that  $F_{\mathcal{N}}(q^2) = F_Z(q^2) \equiv F_V(q^2)$ . The three-momentum transfer ( $q \equiv |\vec{q}|$ ) in terms of the measurable nuclear recoil energy of the target is given by  $q^2 = 2m_N T + T^2 \simeq 2m_N T$ . On the theoretical side, the CE $\nu$ NS cross-section depends on the nuclear matrix element models and the nuclear structure details, which can be introduced through the nuclear form factors for protons and neutrons. In this study, we consider the Helm parametrization for the form factor [101],

$$F_{\text{Helm}}(q^2) = 3 \frac{j_1(qR)}{qR} e^{-\frac{1}{2}q^2 s^2}. \quad (2.5)$$

Here,  $j_1(x) = \sin x/x^2 - \cos x/x$  is the first order Spherical Bessel function. Nuclear radius is given by  $R = \sqrt{c^2 - 5s^2}$ , with the nuclear parameters  $c = 1.2A^{1/3}$  fm,  $s = 0.5$  fm [102].

Although the SM axialvector term in the CE $\nu$ NS cross-section in Eq.(2.2) plays a minor role due to its strong dependence on the nuclear spin, we have nonetheless accounted for it in our analyses. The axial contribution to the SM weak charge,  $Q_{SM_A}$ , is determined through the axialvector form factor  $F_A(q^2)$ , derived from nuclear spin structure function calculations, which describe the momentum dependence of the nuclear spin response in scattering processes, as detailed in Ref. [103],

$$F_A(q^2) = \frac{8\pi}{2J+1} \left[ (g_A^0)^2 S_{00}^T(q^2) + g_A^0 g_A^1 S_{01}^T(q^2) + (g_A^1)^2 S_{11}^T(q^2) \right], \quad (2.6)$$

where  $J$  is the total angular momentum of the nucleus in its ground state,  $S_{ij}^T(q^2)$  is the transverse spin structure function, and  $g_A^0$  and  $g_A^1$  are the isoscalar and isovector axial coupling coefficients, respectively. In the SM case, only  $S_{11}^T(q^2)$  term contributes. The isovector coefficients is given by,

$$g_A^1 = \frac{g_p^A - g_n^A}{2} = \Delta_u^p - \Delta_d^p = \Delta_d^n - \Delta_u^n, \quad (2.7)$$

where,  $\Delta_q^{n=p}$  represents the contribution of the quark-spin content of the nucleon  $n$ . The axial coupling coefficients are defined as  $g_n^A = \Delta_u^n - \Delta_d^n$  with  $g_p^A = -g_n^A$ . Neglecting strangeness and two-body currents, the axial

vector contribution to the SM weak charge can be expressed as,

$$Q_{SM_A}^2 = \frac{8\pi}{2J+1} (\Delta_u^p - \Delta_d^p)^2 S_{11}^T(q^2). \quad (2.8)$$

The numerical values of coefficients are  $\Delta_u^p = \Delta_d^n = 0.842$ , and  $\Delta_d^p = \Delta_u^n = -0.427$  [103, 104]. The most common stable Ge isotopes considered, along with their natural abundances, are  $^{70}\text{Ge}$  (20.8%),  $^{72}\text{Ge}$  (27.5%),  $^{73}\text{Ge}$  (7.8%),  $^{74}\text{Ge}$  (36.5%), and  $^{76}\text{Ge}$  (6.2%). Among these, only  $^{73}\text{Ge}$  has a nonzero nuclear spin ( $J = 9/2$ ); the others have  $J = 0$  due to their even numbers of protons and neutrons. The axialvector contribution to the cross-section vanishes for spin-zero nuclei.

### A. New Light Mediators from Simplified Model

To parametrise new physics at a very low scale, the light mediator models are constructed to include only a few new particles and interactions in general vector, axialvector, scalar, pseudoscalar and tensor form [48, 105]. The appearance of new interactions in the CE $\nu$ NS process is illustrated in Fig. 2. These are so-called simplified models that have been also intensively studied in the dark matter searches at the LHC [106]. For measurements of neutrino-electron scattering or neutrino-nucleus scattering, such models are of interest because the mediators can have a pronounced effect on the recorded recoil spectra, most notably for mediator masses smaller than the maximum momentum transfer. The Lagrangians responsible for these interactions are

$$\begin{aligned} \mathcal{L}_V &\supset [g_{V\nu} \bar{\nu}_L \gamma^\mu \nu_L + g_{Vq} \bar{q} \gamma^\mu q] V_\mu, \\ \mathcal{L}_A &\supset [g_{A\nu} \bar{\nu}_L \gamma^\mu \nu_L - g_{Aq} \bar{q} \gamma^\mu \gamma^5 q] A_\mu, \\ \mathcal{L}_S &\supset [(g_{S\nu} \bar{\nu}_R \nu_L + h.c.) + g_{Sq} \bar{q} q] S, \\ \mathcal{L}_P &\supset [(g_{P\nu} \bar{\nu}_R \nu_L + h.c.) - i g_{Pq} \bar{q} \gamma^5 q] P, \\ \mathcal{L}_T &\supset [g_{T\nu} \bar{\nu}_R \sigma^{\mu\nu} \nu_L - g_{Tq} \bar{q} \sigma^{\mu\nu} q] T_{\mu\nu}, \end{aligned} \quad (2.9)$$

where  $\sigma_{\mu\nu} = \frac{i}{2} [\gamma_\mu, \gamma_\nu] = \frac{i}{2} (\gamma_\mu \gamma_\nu - \gamma_\nu \gamma_\mu)$ . With these Lagrangians, we can match the new mediator interactions from the quark level to the nuclear scale. We find the following for each interaction type:

$$\mathcal{L}_{XN} = g_{XN} \bar{N} N X, \quad (2.10)$$

where  $X = V, A, S, P, T$ . The coupling of the new mediators with nucleus for vector, scalar and pseudoscalar interactions can simply be written as,

$$\begin{aligned} g_{VN} &= \left[ \mathcal{Z} \sum_q Q_q^p g_{Vq} + \mathcal{N} \sum_q Q_q^n g_{Vq} \right] F_V(q^2), \\ g_{SN} &= \left[ \mathcal{Z} \sum_q g_{Sq} \frac{m_p}{m_q} f_{Tq}^p + \mathcal{N} \sum_q g_{Sq} \frac{m_n}{m_q} f_{Tq}^n \right] F_S(q^2), \\ g_{PN} &= \left[ \mathcal{Z} \sum_q g_{Pq} \frac{m_p}{m_q} \Delta_q^p + \mathcal{N} \sum_q g_{Pq} \frac{m_n}{m_q} \Delta_q^n \right] \\ &\quad \times \left( 1 - \sum_{q'} \frac{\bar{m}}{m_{q'}} \right) F_P(q^2), \end{aligned} \quad (2.11)$$

where  $\bar{m}$  is constant defined as  $\bar{m} = (1/m_u + 1/m_d + 1/m_s)^{-1}$  [107, 108]. Here, the spin dependence of the pseudoscalar interaction is neglected, given that its cross-section is suppressed by the recoil energy, and the associated spin contribution is sub-dominant [99].

For axialvector and tensor interactions the definitions of the coupling constants can be expressed in terms of individual form factor which include spin structure functions. In the context of NSI, the relevant spin structure function is  $S_{00}^T(q^2)$ . In the case of tensor interactions, the longitudinal component of the spin structure function,  $S_{00}^L(q^2)$ , also contributes and should be included in the analysis. The axialvector and tensor quark couplings satisfy the relations  $g_{Au} = g_{Ad} \equiv g_{Aq}$  and  $g_{Tu} = g_{Td} \equiv g_{Tq}$ , respectively. Following the definition in Eq (2.6), the effective couplings at the nucleus level can be expressed as,

$$\begin{aligned} g_{AN} &= \sqrt{\frac{8\pi}{2J+1}} \left[ g_{Aq}(\Delta_u^p + \Delta_d^p) \right], \\ g_{TN} &= \sqrt{\frac{8\pi}{2J+1}} \left[ g_{Tq}(\delta_u^p + \delta_d^p) \right]. \end{aligned} \quad (2.12)$$

The parameters in Eqs. (2.11) and (2.12) are listed in Table I. It is worth noting that values for parameters involving strange quarks can be found in the literature [103, 104]; however, we have observed that their impact on our calculations for the NSI of CE $\nu$ NS is negligible. Therefore, we only consider the first lepton family quarks, namely the up and down quarks. In addition, we emphasize that the pseudoscalar interaction with the nucleus was considered negligible in previous works [105, 109, 110], whereas in this study, we incorporate this interaction into our analysis to provide a more comprehensive treatment. Furthermore, while tensor and axialvector interactions are evaluated using the form factors derived from nuclear spin structure functions, we retain the Helm form factor parametrization from Eq. (2.5) for vector, scalar, and pseudoscalar interactions.

TABLE I. Values of the parameters for simplified models.

Parameter	Value	Reference
$m_u$	2.16	[1]
$m_d$	4.67	
$m_s$	93.4	
$m_n$	939.6	
$m_p$	938.3	
$Q_u^p = Q_d^n$	2	[61]
$Q_u^n = Q_d^p$	1	
$f_{T_u}^p$	0.0208	[103, 111]
$f_{T_u}^n$	0.0411	
$f_{T_d}^p$	0.0189	
$f_{T_d}^n$	0.0451	
$\Delta_u^p = \Delta_d^n$	0.842	[103, 104]
$\Delta_u^n = \Delta_d^p$	-0.427	
$\delta_u^p = \delta_d^n$	0.784	[103, 112]
$\delta_u^n = \delta_d^p$	-0.204	

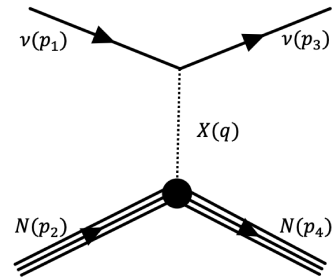


FIG. 2. Representative Feynman diagram for CE $\nu$ NS process with new mediator X.

Based on these considerations, we obtain the differential cross-sections for the case of:

(i) Vector Interaction,

Vector differential cross-section without interference can be written as

$$\left[ \frac{d\sigma}{dT_N} \right]_V = \frac{G_F^2 m_N}{4\pi} \frac{2Q_V^2}{(m_V^2 + 2m_N T_N)^2} \mathcal{K}_V. \quad (2.13)$$

The interference term of the vector differential cross-section can be written as

$$\left[ \frac{d\sigma}{dT_N} \right]_{V_{\text{INT}}} = \frac{G_F^2 m_N}{4\pi} \frac{2\sqrt{2}Q_V Q_{\text{SM}V}}{m_V^2 + 2m_N T_N} \mathcal{K}_V. \quad (2.14)$$

(ii) Axialvector Interaction,

$$\left[ \frac{d\sigma}{dT_N} \right]_A = \frac{G_F^2 m_N}{4\pi} \frac{2Q_A^2}{(m_A^2 + 2m_N T_N)^2} S_{00}^T(q^2) \mathcal{K}_A. \quad (2.15)$$

Although the SM CE $\nu$ NS cross-section given in Eq. (2.2) includes an axialvector component, the interference between the SM and axialvector NSI contributions are not considered here since the relevant spin-structure function for the SM case is  $S_{11}^T(q^2)$ , while for the NSI case is  $S_{00}^T(q^2)$  [103, 110].

(iii) Scalar Interaction,

$$\left[ \frac{d\sigma}{dT_N} \right]_S = \frac{G_F^2 m_N}{4\pi} \frac{Q_S^2}{(m_S^2 + 2m_N T_N)^2} \mathcal{K}_S, \quad (2.16)$$

where  $\mathcal{K}_S$  can be defined as

$$\mathcal{K}_S = \frac{m_N T_N}{E_\nu^2} + \frac{T_N^2}{2E_\nu^2}. \quad (2.17)$$

(iv) Pseudoscalar Interaction,

$$\left[ \frac{d\sigma}{dT_N} \right]_P = \frac{G_F^2 m_N}{4\pi} \frac{Q_P^2}{(m_P^2 + 2m_N T_N)^2} \mathcal{K}_P, \quad (2.18)$$

where  $\mathcal{K}_P$  can be defined as

$$\mathcal{K}_P = \frac{T_N^2}{2E_\nu^2}. \quad (2.19)$$

(v) Tensor Interaction,

$$\left[ \frac{d\sigma}{dT_N} \right]_T = \frac{G_F^2 m_N}{4\pi} \frac{Q_T^2}{(m_T^2 + 2m_N T_N)^2} \times \left[ 8S_{00}^T(q^2) \mathcal{K}_V + 16S_{00}^L(q^2) \left( 1 - \frac{T_N}{E_\nu} \right) \right]. \quad (2.20)$$

In all these equations the new charges  $Q_X$  can be defined as,

$$Q_X = \frac{g_{X\nu} g_{XN}}{G_F}, \quad (2.21)$$

where  $X$  stands for the different interaction channels of V, A, S, P, and T.

### B. Model Independent Non-Standard Interactions of Neutrino

One of the most extensively studied models in the search of new physics BSM is the NSI of neutrinos [113]. NSI of neutrinos, in a model-independent approach, can be described as a four-Fermi point-like interaction, as shown in Fig. 3. This model introduces a new type of contact interaction between neutrinos and matter that differs from the SM theory [51]. In general, NSI can induce a neutral current (NC) and charge current (CC) processes, each implying the presence of a new mediator with heavier mass [114] or in the same order as the EW theory [115]. For CE $\nu$ NS, only the NC case is relevant. Neutrinos with NSI influence quarks inside a nucleus, interacting either as a non-universal flavor-conserving (FC) or flavor-violating (FV) process. In general, the Lagrangians given in terms of model-independent coupling constant in Eq. (2.9) can be modified to define the model-independent NSI by replacing the coupling  $g_X$  with  $\varepsilon$  using the relation given in Eq. (2.24). Specifically, the V-A type for model-independent NSI can be formulated as

$$-\mathcal{L}_{NSI}^{eff} = \varepsilon_{\alpha\beta}^{fP} 2\sqrt{2}G_F (\bar{\nu}_\alpha \gamma_\mu L \nu_\beta) (\bar{f}' \gamma^\mu P f), \quad (2.22)$$

with  $\varepsilon_{\alpha\beta}^{fP}$  is the coupling that describes the strength of the NSI,  $f$  is a first generation SM fermion (e, u, or d) in which  $f = f'$  refers to NC NSI, whereas CC NSI are obtained for  $f' \neq f$ ,  $P$  denotes the chiral projector  $L, R = (1 \pm \gamma^5)/2$ ,  $\alpha$  and  $\beta$  denote the neutrino flavor (e,  $\mu$ , or  $\tau$ ).

The relevant Lagrangian for CE $\nu$ NS NC process can be written as

$$-\mathcal{L}_{NSI}^{eff} = \frac{G_F}{\sqrt{2}} [\bar{\nu}_\alpha \gamma_\mu (1 - \gamma^5) \nu_\beta] [\bar{f} \gamma^\mu (\varepsilon_{\alpha\beta}^{fV} - \varepsilon_{\alpha\beta}^{fA} \gamma^5) f]. \quad (2.23)$$

The NSI coupling  $\varepsilon_{\alpha\beta}^{fX}$  can be expressed as

$$\varepsilon_{\alpha\beta}^{fX} \simeq \frac{g_{X\nu} g_{XN}}{\sqrt{2}G_F M_X^2}, \quad (2.24)$$

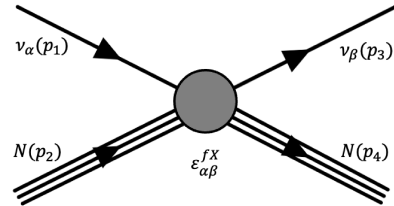


FIG. 3. The Feynman diagram for four-Fermi point-like interaction.

where  $g_X$  and  $m_X$  stand for the coupling constant and mass of the mediator, respectively.

Hence, the differential cross-section of NSI can be written as:

(i) for the vector case

$$\left[ \frac{d\sigma}{dT_N} \right]_V^{NSI} = \frac{G_F^2 m_N}{\pi} |F_V(q^2)|^2 \left[ \varepsilon_{\alpha\beta}^{uV} (\mathcal{N} + 2\mathcal{Z}) + \varepsilon_{\alpha\beta}^{dV} (2\mathcal{N} + \mathcal{Z}) \right]^2 \mathcal{K}_V, \quad (2.25)$$

where  $\alpha = \beta = e, \mu, \tau$  is corresponding to FC type of interaction and  $\alpha \neq \beta = e, \mu, \tau$  is corresponding to FV case.

The interference term for the FC case only can be written as

$$\left[ \frac{d\sigma}{dT_N} \right]_{VINT}^{FC} = \frac{G_F^2 m_N}{\pi} |F_V(q^2)|^2 \times \left[ \varepsilon_{\alpha\alpha}^{uV} (\mathcal{N} + 2\mathcal{Z}) + \varepsilon_{\alpha\alpha}^{dV} (2\mathcal{N} + \mathcal{Z}) \right] \times \left[ (1 - 4 \sin^2 \theta_W) \mathcal{Z} - \mathcal{N} \right] \mathcal{K}_V, \quad (2.26)$$

for the axialvector case;

$$\left[ \frac{d\sigma}{dT_N} \right]_A^{NSI} = \frac{G_F^2 m_N}{\pi} \left( \frac{8\pi}{2J+1} \right) \times \frac{1}{4} \left[ \varepsilon_{\alpha\beta}^{uA} \left( \Delta_u^p \sqrt{S_p^T(q^2)} + \Delta_u^n \sqrt{S_n^T(q^2)} \right) + \varepsilon_{\alpha\beta}^{dA} \left( \Delta_d^p \sqrt{S_p^T(q^2)} + \Delta_d^n \sqrt{S_n^T(q^2)} \right) \right]^2 \mathcal{K}_A, \quad (2.27)$$

where  $S_n^T(q^2)$  denotes the transverse spin structure functions in proton/neutron basis, with  $\mathbf{n} = p, n$ . In this section, we adopt the proton/neutron basis, which enables a clearer identification and evaluation of the individual spin-dependent contributions from protons and neutrons, and provides a more direct connection to the associated quark-level NSI couplings. For a detailed analysis and discussion of this formulation, see Ref. [103].

(ii) for the scalar case;

$$\begin{aligned} \left[ \frac{d\sigma}{dT_N} \right]_S^{NSI} &= \frac{G_F^2 m_N}{2\pi} |F_S(q^2)|^2 \\ &\times \left[ \varepsilon_{\alpha\beta}^{uS} \left( \mathcal{N} \frac{m_n}{m_u} f_{Tu}^n + \mathcal{Z} \frac{m_p}{m_u} f_{Tu}^p \right) \right. \\ &\quad \left. + \varepsilon_{\alpha\beta}^{dS} \left( \mathcal{N} \frac{m_n}{m_d} f_{Td}^n + \mathcal{Z} \frac{m_p}{m_d} f_{Td}^p \right) \right]^2 \mathcal{K}_S. \end{aligned} \quad (2.28)$$

(iii) for the pseudoscalar case;

$$\begin{aligned} \left[ \frac{d\sigma}{dT_N} \right]_P^{NSI} &= \frac{G_F^2 m_N}{2\pi} |F_P(q^2)|^2 \\ &\times \left[ \varepsilon_{\alpha\beta}^{uP} \left( \mathcal{N} \frac{m_n}{m_u} \Delta_u^n + \mathcal{Z} \frac{m_p}{m_u} \Delta_u^p \right) \right. \\ &\quad \left. + \varepsilon_{\alpha\beta}^{dP} \left( \mathcal{N} \frac{m_n}{m_d} \Delta_d^n + \mathcal{Z} \frac{m_p}{m_d} \Delta_d^p \right) \right]^2 \\ &\times \left( 1 - \sum_{q'} \frac{\bar{m}}{m_{q'}} \right)^2 \mathcal{K}_P. \end{aligned} \quad (2.29)$$

(iv) for the tensor case;

$$\begin{aligned} \left[ \frac{d\sigma}{dT_N} \right]_T^{NSI} &= \frac{G_F^2 m_N}{\pi} \left( \frac{8\pi}{2J+1} \right) \\ &\times \left\{ \left[ \varepsilon_{\alpha\beta}^{uT} \left( \delta_u^p \sqrt{S_p^T(q^2)} + \delta_u^n \sqrt{S_n^T(q^2)} \right) \right. \right. \\ &\quad \left. + \varepsilon_{\alpha\beta}^{dT} \left( \delta_d^p \sqrt{S_p^T(q^2)} + \delta_d^n \sqrt{S_n^T(q^2)} \right) \right]^2 \mathcal{K}_V \\ &\quad \left. + \left[ \varepsilon_{\alpha\beta}^{uT} \left( \delta_u^p \sqrt{S_p^L(q^2)} + \delta_u^n \sqrt{S_n^L(q^2)} \right) \right. \right. \\ &\quad \left. \left. + \varepsilon_{\alpha\beta}^{dT} \left( \delta_d^p \sqrt{S_p^L(q^2)} + \delta_d^n \sqrt{S_n^L(q^2)} \right) \right]^2 \left( 2 - \frac{2T_N}{E_\nu} \right) \right\}, \end{aligned} \quad (2.30)$$

where  $S_n^T(q^2)$  and  $S_n^L(q^2)$  denote the transverse and longitudinal spin structure functions in proton/neutron basis, respectively. We follow a similar notation as in the axialvector case. For tensor NSI, both transverse and longitudinal spin structure functions contribute to the cross-section [103].

### C. Exotic Neutral Currents In Coherent $\nu$ -N Scattering

Apart from the model-independent NSI in epsilon-space  $\varepsilon_{\alpha\beta}^{qX}$  additional, more “exotic” new interactions could be presented. Five possible types of such “exotic” interactions can be introduced namely vector (V), axialvector (A), scalar (S), pseudoscalar (P), and tensor (T). The Lagrangian at the quark level for these interactions, considering all Lorentz-invariant interactions of

neutrinos with first generation quarks, can be formulated as:

$$\mathcal{L} = \frac{G_F}{\sqrt{2}} \sum_X \bar{\nu} \Gamma^X \nu \left[ \bar{q} \Gamma^X (C_X^q + i\gamma^5 D_X^q) q \right]. \quad (2.31)$$

We only consider first generation of quarks, where  $q$  stands for u and d quarks, and  $\Gamma^X$  can be described as

$$\Gamma^X = \{ \gamma^\mu, \gamma^\mu \gamma^5, I, i\gamma^5, \sigma^{\mu\nu} \}. \quad (2.32)$$

Here  $X$  represents for V, A, S, P, and T.

Analogous to Eq. (2.24), the coefficients  $C_X^q$  and  $D_X^q$  are expected to be of the order  $(g_X^2/g^2)(m_W^2/m_X^2)$ , where  $m_X$  represents the mass of the new exchange particles and  $g_X$  denotes their coupling constants. The coefficients  $C_X^q$  and  $D_X^q$  in Eq. (2.31) are dimensionless and, in principle, can be complex numbers. However for simplicity, we assume these parameters  $C_X^q$  and  $D_X^q$  to be real [50].

The effective Lagrangian of neutrino-nucleus interaction, transition from the quark level to the nucleus scale, can be expressed as,

$$\begin{aligned} \mathcal{L}_{\nu-N} \supset &\sum_{X=S,V,T} \bar{\nu} \Gamma^X \nu \left[ \bar{N} C_X \Gamma^X N \right] \\ &+ \sum_{(X,Y)=(S,P),(V,A)} \bar{\nu} \Gamma^X \nu \left[ \bar{N} i D_X \Gamma^Y N \right]. \end{aligned} \quad (2.33)$$

Here the expression for  $C_X$  and  $D_X$  can be derived from Eqs. (2.11) and (2.12). It is worth noting that different notation for the couplings ( $g_{XN}$ ) was used in Section II A. The notation adopted here follows the same conventions in Ref. [75].

Since the effective couplings for nuclear spin-dependent interactions are determined by the sum over spin-up and spin-down nucleons, axial and pseudoscalar currents are suppressed in heavy nuclei. Consequently, the most significant contributions are expected from scalar, vector and tensor quark currents. As such, we can constraint the quark currents can be considered as  $C_S^q$ ,  $D_P^q$ ,  $C_V^q$ ,  $D_A^q$ , and  $C_T^q$ . The expression for  $D_P$  can be obtained from that of  $C_S$  by replacing  $C_S^q$  with  $D_P^q$ , while  $D_A$  can be derived from  $C_V$  by substituting  $C_V^q$  with  $D_A^q$  [75, 76].

$$\begin{aligned} \left[ \frac{d\sigma}{dT_N} \right]_{EXO} &= \frac{G_F^2 m_N}{4\pi} |F(q^2)|^2 \mathcal{N}^2 \left[ (\xi_V + \xi_{SM})^2 \mathcal{K}_V \right. \\ &\quad \left. + \xi_A^2 \mathcal{K}_A - 2\xi_V \xi_A \mathcal{K}_{VA} + \xi_S^2 \mathcal{K}_S \right. \\ &\quad \left. + \xi_T^2 \mathcal{K}_T - R \mathcal{K}_{VA} \right], \end{aligned} \quad (2.34)$$

where  $\mathcal{K}_T$  and  $\mathcal{K}_{VA}$  are

$$\begin{aligned} \mathcal{K}_T &= 1 - \frac{m_N T_N}{4E_\nu^2} - \frac{T_N}{E_\nu} + \frac{T_N^2}{4E_\nu^2}, \\ \mathcal{K}_{VA} &= \frac{T_N^2}{2E_\nu^2} - \frac{T_N}{E_\nu}, \end{aligned} \quad (2.35)$$

and the new exotic couplings can be defined in terms of the coefficients  $C_X$  and  $D_X$  as

$$\begin{aligned}\xi_V^2 &= \frac{C_V^2 + D_A^2}{\mathcal{N}^2} \\ \xi_A^2 &= \frac{D_V^2 + C_A^2}{\mathcal{N}^2} \\ \xi_V \xi_A &= \frac{C_V D_V + C_A D_A}{\mathcal{N}^2} \\ \xi_S^2 &= \frac{C_S^2 + D_P^2}{\mathcal{N}^2} \\ \xi_T^2 &= 8 \frac{C_T^2 + D_T^2}{\mathcal{N}^2} \\ R &= 2 \frac{C_P C_T - C_S C_T + D_T D_P - D_T D_S}{\mathcal{N}^2}.\end{aligned}\quad (2.36)$$

While different notations exist in the literature to represent the SM contribution [75, 76], we adopt the convention used in Refs. [67, 71]. Specifically,  $\xi_{\text{SM}} = [\mathcal{Z}(1 - 4\sin^2\theta_W) - \mathcal{N}]/\mathcal{N}$  is used to represent the SM contribution in Eq. (2.34). The first two lines of Eq. (2.34) encompass the vector interaction including the SM contribution, the axialvector interaction, the scalar interaction, which involves interference with pseudoscalar terms. The last line includes the tensor interaction, while the R term accounts for the interference between the (pseudo-) scalar and tensor interactions.

### III. EXPERIMENTAL DATA AND EVENT RATES

The number of events can be calculated from

$$R_X = N_{\text{tar}} \int_{T_{N_{\text{min}}}}^{T_{N_{\text{max}}}} dT_N \int_{E_{\nu_{\text{min}}}}^{E_{\nu_{\text{max}}}} dE_\nu \frac{d\Phi}{dE_\nu} \left[ \frac{d\sigma}{dT_N} \right]_X, \quad (3.1)$$

where  $X$  represents different interaction channels such as the SM, NSI, etc.,  $d\Phi/dE_\nu$  is the neutrino spectra shown in Fig. 4,  $d\sigma/dT_N$  is differential cross-section of the process, and  $N_{\text{tar}}$  is the total number of target nuclei.

A nuclear recoil threshold of  $T_{N_{\text{min}}} \simeq 2.96$  eV is the minimum required average ionization energy in Ge to detect neutrinos with energy  $E_\nu$ . From kinematics, the maximum recoil energy is defined as  $T_{N_{\text{max}}} = 2E_\nu^2/(m_N + 2E_\nu) \simeq 2E_\nu^2/m_N$ . Here  $E_\nu$  is running from 0 to  $\sim 8$  MeV with 10 keV bin-size.

Scattering of neutrinos off nuclei provides a valuable opportunity to test the SM and to explore potential new physics BSM through various experimental programs. In particular, nuclear reactors and SNS serve as optimal facilities for studying CE $\nu$ NS processes [9, 13, 116]. SNS-based neutrino sources, generated from pion and muon decays at rest (DAR- $\pi$ ), offer a complementary flux in the intermediate-energy range [9]. Meanwhile, nuclear reactors produce significantly larger electron antineutrino fluxes ( $\bar{\nu}_e$ ) in the low-energy regime compared to other neutrino sources, making them well-suited for precision

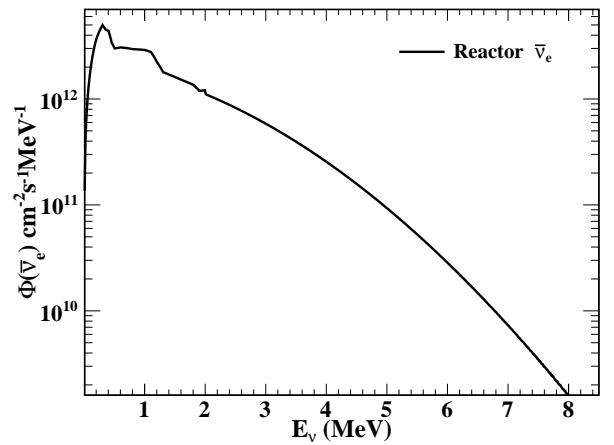


FIG. 4. A typical neutrino spectrum ( $\Phi_\nu$ ) for reactor  $\bar{\nu}_e$  corresponding to a total flux of  $6.35 \times 10^{12} \text{ cm}^{-2} \text{ s}^{-1}$  at the detector site (see Fig. 5b in Ref. [117].)

measurements. The TEXONO experiment, utilizing low-threshold detectors, plays a crucial role in probing neutrino interactions and searching for potential NSI effects through reactor-based neutrino experiments. The reactor  $\bar{\nu}_e$  spectrum used in our analysis shown in Fig. 4 is derived from the total spectrum at the typical reactor operation conditions, as given in Fig. 5b in Ref. [117]. The total  $\bar{\nu}_e$ -flux is determined by the reactor thermal power, i.e.  $\Phi(\bar{\nu}_e) = 6.35 \times 10^{12} \text{ cm}^{-2} \text{ s}^{-1}$  at the experimental site. This value carries a conservative uncertainty of 5%, consistent with those used in similar reactor-based experiments [87, 118, 119]. This spectrum is used to calculate the expected recoil spectra throughout our analysis.

As part of this effort, the TEXONO Collaboration is conducting an intense research program on low-energy neutrino physics ( $< 10$  MeV) at the Kuo-Sheng Nuclear Power Plant in Taiwan. The collaboration conducted an experiment in 2016 using a high-purity n-type point-contact germanium (nPC-Ge) detector cooled by liquid nitrogen and upgraded its facilities in 2024 with an advanced p-type point-contact germanium (pPC-Ge) detector. In the present study, 124.2(70.3) kg-days reactor ON(OFF) data collected at Kuo-Sheng Neutrino Laboratory (KSNL) with a threshold energy of 300 eV [86], and 242(357) kg-days reactor ON(OFF) data with an improved threshold energy of 200 eV [87] are analysed.

In order to predict the number of observable events in the detectors, it is essential to account for detector quenching, resolution, and detection efficiency functions. First, the nuclear recoil energy  $T_N$  must be converted into the electron-equivalent energy  $E_{ee}$  using the quenching function,  $Q_F$ , such that

$$E_{ee} = Q_F(T_N) \times T_N. \quad (3.2)$$

Then the differential cross-section of  $d\sigma/dT_N$  can be con-

verted into  $d\sigma/dE_{ee}$  by

$$\begin{aligned} \frac{d\sigma}{dE_{ee}} &= \left( \frac{d\sigma}{dT_N} \right) / \left( \frac{dE_{ee}}{dT_N} \right) \\ &= \left( \frac{d\sigma}{dT_N} \right) / \left( \frac{dQ_F}{dT_N} T_N + Q_F \right). \end{aligned} \quad (3.3)$$

Subsequently, the predicted electron-equivalent energy  $E_{ee}$  must be smeared by energy resolution function in order to transform the calculated event rate into the observable event rate within specific energy bins. Finally, the predicted event rate must be processed through the detector efficiency function to align the predicted and observed rates, ensuring they are directly comparable.

The  $Q_F$  for the TEXONO HPGe detector is provided using the standard Lindhard Model, expressed as

$$Q_F = \frac{k g(\epsilon)}{1 + k g(\epsilon)}, \quad (3.4)$$

where  $g(\epsilon)$  is from fitting by [120] with the function of

$$g(\epsilon) = 3\epsilon^{0.15} + 0.7\epsilon^{0.6} + \epsilon, \quad (3.5)$$

where  $\epsilon = 11.5 Z^{-7/3} T_N$ , with  $T_N$  in keV, and  $k$  is a measure of the electronic energy loss. There are some intense effort on quantifying the impact of quenching factor uncertainties on CE $\nu$ NS cross-section measurement with germanium detector [121, 122]. In the latest study with pPC-Ge detector, the TEXONO collaboration chose Lindhard model with parameter  $k \approx 0.162$  [87].

Energy resolution function is described as a Gaussian energy resolution function given as

$$\sigma^2 = \sigma_o^2 + E_{ee}\eta F, \quad (3.6)$$

where  $\sigma_o$ , obtained by Root-Mean-Square (RMS) of test-pulsar, is  $49 eV_{ee}$  for the nPC-Ge detector and  $31.37 eV_{ee}$  for pPC-Ge detector,  $\eta = 2.96 eV_{ee}$  is the average energy required for photons to create an electron-hole pair in Ge, and  $F \approx 0.105$  is the Fano factor taken from Ref. [119].

## IV. ANALYSIS AND RESULTS

### A. Event Rate Predictions

In this section, we present our analysis results obtained from TEXONO nPC-Ge(2016) and pPC-Ge(2025) data for each model considered.

To constrain the parameters, we adapt the analysis method based on the minimum  $\chi^2$ -method. The TEXONO nPC-Ge data from 2016 and upgraded pPC-Ge from 2025 data are analysed using a 1-bin analysis by minimizing

$$\chi^2 = \sum_i \left[ \frac{R_{\text{expt}}(i) - R_{\text{SM}}(i) - R_X(i)}{\Delta(i)} \right]^2, \quad (4.1)$$

TABLE II. Summary of 90% CL upper limits on the coupling constant parameter for V, A, S, P, and T type NSI interactions, obtained from TEXONO nPC-Ge (2016) and pPC-Ge (2025) experimental data, for both  $m_X^2 \ll 2m_N T_N$  and  $m_X^2 \gg 2m_N T_N$  scenarios.

	$(m_X^2 \ll 2m_N T_N)$		$(m_X^2 \gg 2m_N T_N)$		
Fitting Par.	TEXONO( $\times 10^{-5}$ ) nPC-Ge	TEXONO( $\times 10^{-6}$ ) pPC-Ge	Fitting Par	TEXONO( $\times 10^{-6}$ ) nPC-Ge	TEXONO( $\times 10^{-6}$ ) pPC-Ge
$g_V$	< 5.54	< 2.57	$g_V/m_V$	< 4.24	< 2.18
$g_A$	< 148.5	< 61.3	$g_A/m_A$	< 108.7	< 50.39
$g_S$	< 1.33	< 0.56	$g_S/m_S$	< 0.97	< 0.46
$g_P$	< 412.3	< 183.0	$g_P/m_P$	< 296.6	< 147.1
$g_T$	< 100.8	< 41.2	$g_T/m_T$	< 74.2	< 34.02

where  $R_{\text{expt}}$  is the measured residual event rate,  $R_{\text{SM}}$  and  $R_X$  are the expected event rates for the SM and  $X$  represents V, A, S, P, and T, respectively; and  $\Delta$  is the  $i^{\text{th}}$  bin statistical uncertainty published by the experiments.

Event rates as a function of recoil energy  $T_N$  for V, A, S, P, and T type NSI are shown in Fig. 5. These are calculated using the data from the TEXONO pPC-Ge experiment, based on specific values of mass and coupling constant parameters for the simplified model and specific values of  $\epsilon_{ee}^{uX} - \epsilon_{ee}^{dX}$  parameters for the model-independent approach. In Fig. 5, we present the predicted differential event rates for the SM CE $\nu$ NS process (solid-black) alongside possible new interactions considered in both the simplified model (left panel) and the model-independent NSI framework (right panel). The event rates are categorized by interaction type:  $V$  (dotted-light blue),  $V_{+INT}$  (dashed-dark blue),  $A$  (long dashed-magenta),  $S$  (long dash dotted-red),  $P$  (dash double dotted-orange), and  $T$  (dash triple dotted-green). The SM differential event rates are calculated using Eq. (3.1), while the corresponding differential cross-sections are derived from Eq. (2.2). For the NSI differential cross-sections, the equations from Eq. (2.13) to Eq. (2.20) are employed for simplified model and the equations from Eq. (2.25) to Eq. (2.30) are used for the model-independent approach. In this analysis, we consider a mediator mass parameter of  $m_X = 10$  MeV and coupling constants varying in the range  $g_X = 0.1 - 20 \times 10^{-4}$  for each interaction type. The representative values chosen for the coupling constants are as follows:  $g_V = 4 \times 10^{-5}$ ,  $g_A = 8 \times 10^{-4}$ ,  $g_S = 1 \times 10^{-5}$ ,  $g_P = 2 \times 10^{-3}$ , and  $g_T = 6 \times 10^{-4}$ .

We observe that when the recoil energy,  $T_N$ , is below 1 keV for the TEXONO pPC-Ge experiment, the new interactions deviate significantly from the SM and also differ notable from each other. However, as the nuclear recoil energy increases, the new interactions tend to converge towards the SM prediction and, in some cases, overlap with them. This behavior can primarily be attributed to the dependence of the cross-sections on the

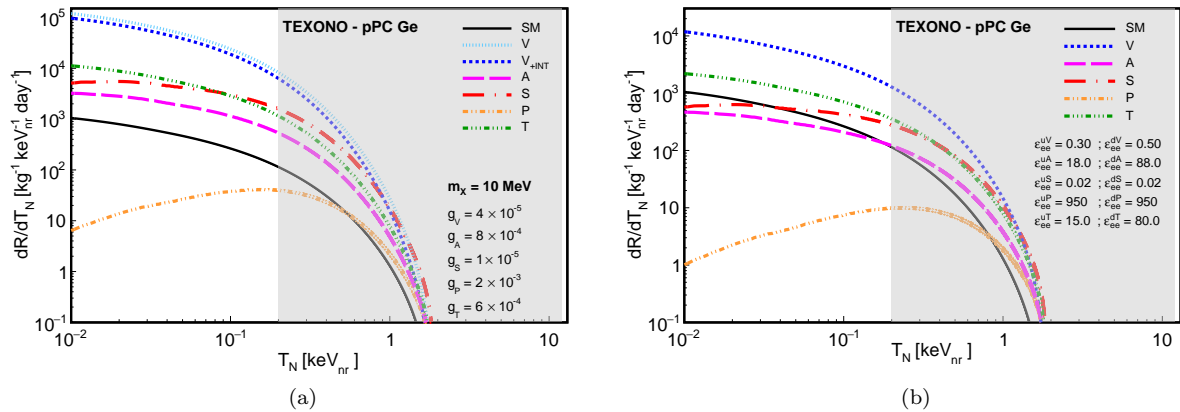


FIG. 5. Event rates as a function of the recoil energy  $T_N$  for V, A, S, P, and T type NSI with typical neutrino spectra for (a) specific values of mass and coupling, and for (b) specific values of  $\varepsilon_{ee}^{uX} - \varepsilon_{ee}^{dX}$  parameters. These values are presented for the TEXONO pPC–Ge [87] data.  $V_{+INT}$  represents to V type NSI with interference with the SM. The gray-shaded regions indicate the region-of-interest (ROI) for each experiment.

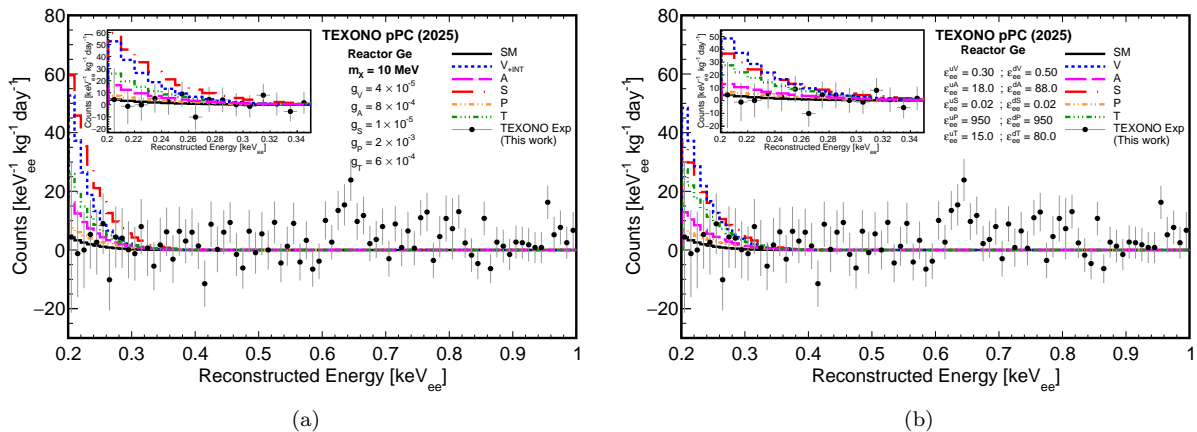


FIG. 6. Residual and expected event rate for specific values of (a) mass and coupling, and (b)  $\varepsilon_{ee}^{uX} - \varepsilon_{ee}^{dX}$  parameters for the TEXONO pPC–Ge experiment with the SM prediction superimposed. These predictions incorporate quenching factor and response function provided by the TEXONO Collaboration [87]. The dotted, dashed, long-dashed, long-dash-dotted, dash-double-dotted, and dash-triple-dotted histograms represent the expected event rates for various NSI scenarios.

square of the  $2m_N T_N$  term in the denominator. As the nuclear recoil energy decreases, this term becomes dominant, leading to a rapid increase in the cross-sections for the new interactions. Consequently, the spectra of these interactions behave differently from the SM prediction, with the divergence becoming more pronounced at lower nuclear recoil energies.

For model-independent NSI, we identify values near the best-fit points for all possible new interaction types in scenarios where two epsilon parameters are present simultaneously. As a reference, we present the  $\varepsilon_{ee}^{uX} - \varepsilon_{ee}^{dX}$  case in Fig. 5 (right panel). The values adopted to generate this reference plot are as follows:  $\varepsilon_{ee}^{uV} = 0.30$ ,  $\varepsilon_{ee}^{dV} = 0.50$ ,  $\varepsilon_{ee}^{uA} = 18.0$ ,  $\varepsilon_{ee}^{dA} = 88.0$ ,  $\varepsilon_{ee}^{uS} = 0.02$ ,  $\varepsilon_{ee}^{dS} = 0.02$ ,  $\varepsilon_{ee}^{uP} = 950$ ,  $\varepsilon_{ee}^{dP} = 950$ ,  $\varepsilon_{ee}^{uT} = 15.0$ , and  $\varepsilon_{ee}^{dT} = 80.0$ .

We present the expected number of events for the

TEXONO pPC–Ge [87] experiment in Fig. 6, plotted against reconstructed energy ( $\text{keV}_{ee}$ ), with experimental data represented by black dots where the SM event predictions are shown as solid black lines. To explore the effects of NSI on CE $\nu$ NS, we also provide the estimated number of events with specific values in both the mass-coupling (left panel) and  $\varepsilon_{ee}^{uX} - \varepsilon_{ee}^{dX}$  (right panel) parameter spaces.

## B. Bounds from Simplified Model

Eqs. (2.13) – (2.20) indicate that the cross-section for all interaction types depends on the mass and coupling constant in the form of  $g_X^2 / (m_X^2 + 2M_N T_N)$ . Based on this dependence, the resulting limits exhibit distinct

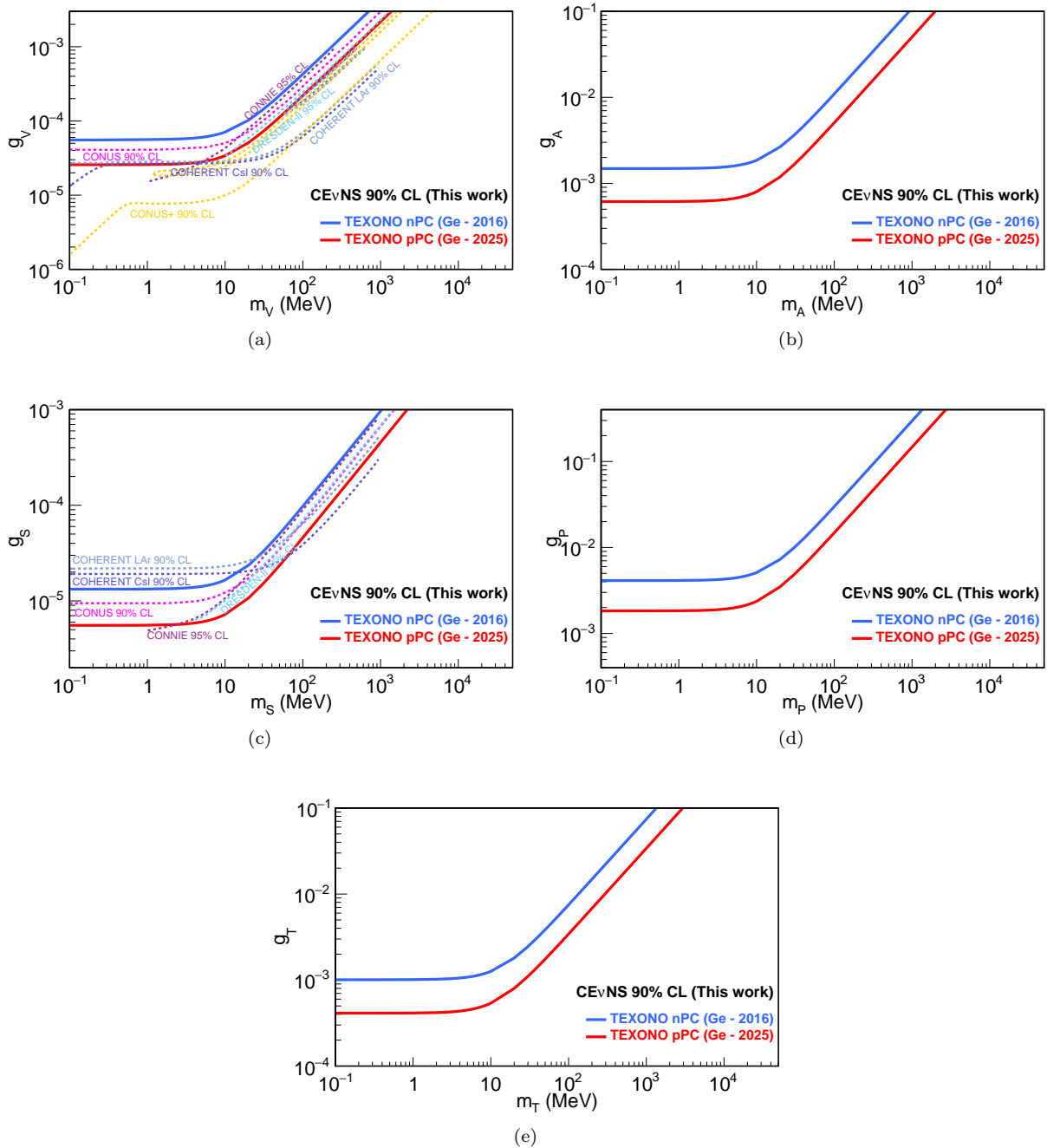


FIG. 7. Bounds at 90% CL are presented for (a) vector, (b) axialvector, (c) scalar, (d) pseudoscalar, and (e) tensor mediator masses and couplings, obtained from the TEXONO nPC–Ge and pPC–Ge experiments comparison with the existing global bounds from various reactor-based experiments, CONUS+ [49], CONUS [57], CONNIE [58], and DRESDEN-II [60], as well as accelerator-based experiments, COHERENT CsI(Na) and LAr [67].

trends: in the low-mass regime ( $m_X \lesssim 10$  MeV), the upper limits are determined solely by the coupling constant  $g_X$ , while in the high-mass regime ( $m_X \gtrsim 10$  MeV), the limits scale with  $g_X/m_X$  (as shown in Figure 7). Taking this behavior into account, Table II provides a summary of the corresponding upper limits at 90% C. L.(CL) for the coupling constant parameters asso-

ciated with V, A, S, P and T type NSI within the simplified model for two distinct mass regimes,  $m_X^2 \ll 2m_N T_N$  and  $m_X^2 \gg 2m_N T_N$ , across the TEXONO nPC–Ge and pPC–Ge experiments. The first two columns of Table II corresponds to the  $m_X^2 \ll 2m_N T_N$  case, and lists the 90% CL upper limits for the coupling constants. The latter two columns represent for  $m_X^2 \gg 2m_N T_N$  case,

and showing the 90% CL upper limits for the slope of  $g_X/m_X$ . Table II highlights the varying sensitivity of each experiment and interaction type, with some coupling constants being more tightly constrained than others. In particular, the upper bounds obtained from the TEXONO pPC–Ge data represent a significant improvement over those obtained from the TEXONO nPC–Ge data, with the scalar interaction providing the most stringent constraint ( $g_S < 0.56 \times 10^{-5}$ ) and the pseudoscalar interaction providing the least stringent constraint ( $g_P < 18.3 \times 10^{-4}$ ).

Building on the results summarized in Table II, Figure 7 offers a detailed visualization of the 90% CL exclusion plots for all possible interaction types (V, A, S, P, and T) in the mass-coupling  $m_X - g_X$  parameter space. These plots illustrate how the upper limits on the coupling constants evolve across different mediator masses. For comparison, the constraints from other reactor-based experiments, such as CONUS+ [12], CONUS [57], CONNIE [58], and Dresden-II [60], as well as from the accelerator-based COHERENT CsI and LAr experiments [67] are superimposed. In Fig. 7a, we see that CONUS+ achieves the most stringent upper limits for vector interactions by combining both CE $\nu$ NS and  $\nu$ ES channels, with a significant improvement in the low mediator mass region. Notably, COHERENT CsI provides the next strongest constraints for mediator masses below  $\sim 0.2$  MeV, also benefiting from the inclusion of  $\nu$ ES. At higher mediator masses, CONNIE provides the second most stringent bounds, followed by TEXONO pPC–Ge, COHERENT CsI, COHERENT LAr, Dresden-II, CONUS, and TEXONO nPC–Ge. In addition, CONUS+, COHERENT CsI, and LAr exhibit allowed regions resulting from parameter degeneracies. These allowed regions appear for mediators' masses greater than 1 MeV for CONUS+, while they appear when masses exceed 30 MeV for COHERENT CsI and LAr. Such degeneracies arise because certain parameter combinations produce indistinguishable effects on the measured event rates. These can be mitigated by combining CE $\nu$ NS data from detectors with different nuclear targets, since varying weak charge dependencies help to break these degeneracies more effectively, leading to stronger and more robust constraints.

Similarly, in Fig. 7c, CONNIE sets the strongest limit for the scalar case, followed by TEXONO pPC–Ge and Dresden-II, respectively. The subsequent limits are given by CONUS, TEXONO nPC–Ge, COHERENT CsI and COHERENT LAr. Although the COHERENT results benefit from the inclusion of the  $\nu$ ES channel, such enhancement is less effective in the scalar case, as the cross-section scales with  $\sim 1/T_N$ , leading to a weaker impact compared to the vector interaction.

For the axialvector and tensor interactions, shown in Figs. 7b and 7e respectively, the constraints are significantly weaker because these interactions depend on the spin of individual nucleons rather than depending on the total number of nucleons. In most nuclei, these spin-

dependent interactions are primarily affected by unpaired nucleons, limiting the coherent enhancement observed in spin-independent interactions, where the cross-section scales with the square of the neutron number. Between these two cases, the tensor interaction produces slightly stronger limits compared to the axial vector due to taking advantage of the distinct recoil energy and spin dependence of the tensor interaction. For the pseudoscalar interaction shown in Fig. 7d the constraints are even less stringent, as its cross-section decreases rapidly at low recoil energies, further weakening the sensitivity. As for the vector and scalar interactions, the scalar interaction, with a cross-section scaling as  $\sim 1/T_N$ , generally provides stronger constraints than the vector interaction, whose cross-section scales as  $\sim 1/T_N^2$  and is thus more strongly suppressed at higher recoil energies. Nonetheless, across all interaction types considered, TEXONO pPC–Ge consistently provides stronger limits than TEXONO nPC–Ge, highlighting the improved performance of the pPC detector set-up.

### C. Bounds from Model-Independent NSI

Table III presents the best-fit measurement results and corresponding limits at 90% CL for individual epsilon parameters in the TEXONO nPC–Ge and pPC–Ge experiments. This analysis assumes one non-zero parameter at a time, with all other parameters set to zero, and the table presents the resulting constraints for both flavor-conserving (FC) and flavor-violating (FV) NSI scenarios. As in the simplified model, five types of interactions are considered: V, A, S, P, and T, with couplings denoted as  $\varepsilon_{\alpha\beta}^{fX}$ , where  $f = u, d$ ;  $\alpha, \beta = e, \mu, \tau$ ; and  $X = V, A, S, P$ , and T. Because the composition of the reactor neutrino flux consists solely of  $\bar{\nu}_e$ , the TEXONO experiment is sensitive only to interactions involving electron neutrino flavor. Assuming real-valued couplings and applying the hermiticity condition  $\varepsilon_{\beta\alpha}^{fX} \equiv (\varepsilon_{\alpha\beta}^{fX})^*$ , the number of independent parameters per quark flavor reduces to six. However, the reactor flux allows constraints on only two of these per flavor. Except for vector NSI, the FC and certain FV couplings are expected to be identical (i.e.,  $\varepsilon_{ee}^{fX} = \varepsilon_{e\mu}^{fX} = \varepsilon_{e\tau}^{fX}$ ). This equivalence arises because the strength of the FC coupling on nuclei corresponds to that of the FV parameter, due to the absence of interference between NSI and the SM and their dependency on the same flux term. Therefore, the relevant coupling parameters in the TEXONO experiment are  $\varepsilon_{ee}^{fX}$  for the FC case and  $\varepsilon_{e\mu(\tau)}^{fX}$  for the FV case.

As summarized in Table III, FV vector couplings provide tighter constraints, while FC couplings remain less constrained due to the destructive nature SM interference term. However, while the presence of SM interference allows well-defined regions to be determined for FC vector couplings, only upper bounds can be determined for FV couplings, as they appear only in quadratic form in the cross-section. NSI couplings associated with the

TABLE III. Summary of the best-fit parameter values (BFPVs) and corresponding limits at  $1\sigma$  and 90% CL for V, A, S, P, and T type NSI measurements, based on one-parameter-at-a-time analysis. The results are presented in comparison with two datasets from the TEXONO Collaboration: nPC–Ge (2016) data and pPC–Ge (2025) datasets. Here only one parameter is assumed to be non-zero for each bound.

Fitting Par	TEXONO nPC–Ge			TEXONO pPC–Ge		
	BFPV $\pm 1\sigma$	90% CL	$\chi^2/\text{dof}$	BFPV $\pm 1\sigma$	90% CL	$\chi^2/\text{dof}$
$\varepsilon_{ee}^{uV}$	$0.18 \pm 1.421$	$-1.71 < \varepsilon_{ee}^{uV} < 2.084$	81.36/120	$0.0004^{+0.527}_{-0.153}$	$-0.223 < \varepsilon_{ee}^{uV} < 0.597$	87.87/79
$\varepsilon_{ee}^{dV}$	$0.17 \pm 1.313$	$-1.58 < \varepsilon_{ee}^{dV} < 1.926$	81.36/120	$0.0004^{+0.487}_{-0.142}$	$-0.206 < \varepsilon_{ee}^{dV} < 0.551$	87.87/79
$(\varepsilon_{e\mu(\tau)}^{uV})^2$	$-0.004 \pm 1.412$	$\varepsilon_{e\mu(\tau)}^{uV} < 1.375$	81.37/120	$(-0.04 \pm 8.1) \times 10^{-2}$	$\varepsilon_{e\mu(\tau)}^{uV} < 0.364$	87.87/79
$(\varepsilon_{e\mu(\tau)}^{dV})^2$	$-0.004 \pm 1.304$	$\varepsilon_{e\mu(\tau)}^{dV} < 1.322$	81.37/120	$(-0.04 \pm 6.9) \times 10^{-2}$	$\varepsilon_{e\mu(\tau)}^{dV} < 0.337$	87.87/79
$(\varepsilon_{ee(\mu;\tau)}^{uA})^2$	$(-0.93 \pm 4.35) \times 10^5$	$\varepsilon_{ee(\mu;\tau)}^{uA} < 788.9$	81.3/120	$(0.12 \pm 2.08) \times 10^4$	$\varepsilon_{ee(\mu;\tau)}^{uA} < 188.4$	87.86/79
$(\varepsilon_{ee(\mu;\tau)}^{dA})^2$	$(-1.88 \pm 8.84) \times 10^4$	$\varepsilon_{ee(\mu;\tau)}^{dA} < 355.8$	81.3/120	$(0.23 \pm 4.24) \times 10^3$	$\varepsilon_{ee(\mu;\tau)}^{dA} < 84.92$	87.86/79
$(\varepsilon_{ee(\mu;\tau)}^{uS})^2$	$(-0.03 \pm 7.8) \times 10^{-2}$	$\varepsilon_{ee(\mu;\tau)}^{uS} < 0.323$	81.37/120	$(0.24 \pm 3.71) \times 10^{-4}$	$\varepsilon_{ee(\mu;\tau)}^{uS} < 0.025$	87.86/79
$(\varepsilon_{ee(\mu;\tau)}^{dS})^2$	$(-0.03 \pm 7.7) \times 10^{-2}$	$\varepsilon_{ee(\mu;\tau)}^{dS} < 0.321$	81.37/120	$(0.22 \pm 3.65) \times 10^{-4}$	$\varepsilon_{ee(\mu;\tau)}^{dS} < 0.024$	87.86/79
$(\varepsilon_{ee(\mu;\tau)}^{uP})^2$	$(-1.40 \pm 6.53) \times 10^7$	$\varepsilon_{ee(\mu;\tau)}^{uP} < 9674.7$	81.32/120	$(0.40 \pm 3.88) \times 10^6$	$\varepsilon_{ee(\mu;\tau)}^{uP} < 2605.0$	87.86/79
$(\varepsilon_{ee(\mu;\tau)}^{dP})^2$	$(-1.44 \pm 6.71) \times 10^7$	$\varepsilon_{ee(\mu;\tau)}^{dP} < 9801.0$	81.32/120	$(0.40 \pm 3.98) \times 10^6$	$\varepsilon_{ee(\mu;\tau)}^{dP} < 2638.2$	87.86/79
$(\varepsilon_{ee(\mu;\tau)}^{uT})^2$	$(-0.25 \pm 1.15) \times 10^6$	$\varepsilon_{ee(\mu;\tau)}^{uT} < 1284.5$	81.32/120	$(0.42 \pm 11.2) \times 10^4$	$\varepsilon_{ee(\mu;\tau)}^{uT} < 433.1$	87.86/79
$(\varepsilon_{ee(\mu;\tau)}^{dT})^2$	$(-0.9 \pm 4.22) \times 10^4$	$\varepsilon_{ee(\mu;\tau)}^{dT} < 245.8$	81.32/120	$(0.86 \pm 19.1) \times 10^2$	$\varepsilon_{ee(\mu;\tau)}^{dT} < 56.80$	87.86/79

other interaction types – A, S, P, and T – are similarly constrained as FV vector couplings, as they do not exhibit interference with the SM. As we see in the Table III, since TEXONO operates with a single-flavor neutrino flux, both FC and FV couplings yield the same constraints in this scenario, except for the vector interactions due to the SM interference. Although the pPC–Ge set-up offers clearly improved bounds over nPC–Ge configuration, reactor neutrino experiments remains limited in its ability to probe various NSI parameters due to its reliance on a single-flavor neutrino flux.

We further explore the sensitivities to pairs of NSI parameters. While a wide variety of NSI parameter pairs can be analysed, our study is limited to a few illustrative cases. These selected examples effectively capture the key features and trends observed across the parameter space. The allowed regions for other parameter combinations generally exhibit similar behavior. By focusing on these representative cases, we provide a clear and concise overview of the parameter space, minimizing redundancy and ensuring the clarity and consistency in this work.

In Figs. 8 and 9, we present the 90% CL bounds for all possible flavor-diagonal (FC) and flavor-off-diagonal (FV) cases of vector NSI interactions. Fig. 8 focuses on single type FC-FC and single type FV-FV parameter spaces, with the left panel showing limits for a scenario involving a single flavor-diagonal term (e.g.,  $\varepsilon_{ee}^{uV} - \varepsilon_{ee}^{dV}$ ), and right panel showing bounds for a scenario involving a

single flavor-off-diagonal term (e.g.,  $\varepsilon_{e\mu}^{uV} - \varepsilon_{e\mu}^{dV}$ ). In both parameter spaces, the constraints appear as diagonal parallel bands; the FV-FV case provide slightly tighter bounds compared to the FC-FC case as it does not interfere with the SM which gives only destructive contribution to the total cross-section. For comparison, we adopt existing bounds from various reactor-based experiments, CONUS [57] and CONUS+ [49], from accelerator-based experiments, COHERENT CsI, LAr [67], and Ge [74], as well as dark matter experiments, XENONnT and PandaX-4T [123] in Fig. 8a. Notably, the COHERENT Ge provides the most stringent limits, with CONUS+ offering the second strongest bound. While accelerator-based experiments continue to be leading contributors, improved constraints from the latest CONUS+ and TEXONO pPC–Ge experiments underscore the growing importance of reactor neutrino experiments. This is driven by increased sensitivities and advancements in detection technologies, which are crucial for studies beyond the SM.

For certain cases, particularly in CONUS+ and COHERENT CsI, in Fig. 8a, degenerate regions emerge due to interference between the SM and NSI differential cross-sections. These degeneracies are exclusive to vector interactions. The degeneracy region appearing in Fig. 8a is a consequence of the dependence of the cross-section on specific linear combinations of the parameters and interference of these parameters with the SM, as derived from Eqs.(2.25), and Eq. (2.26).

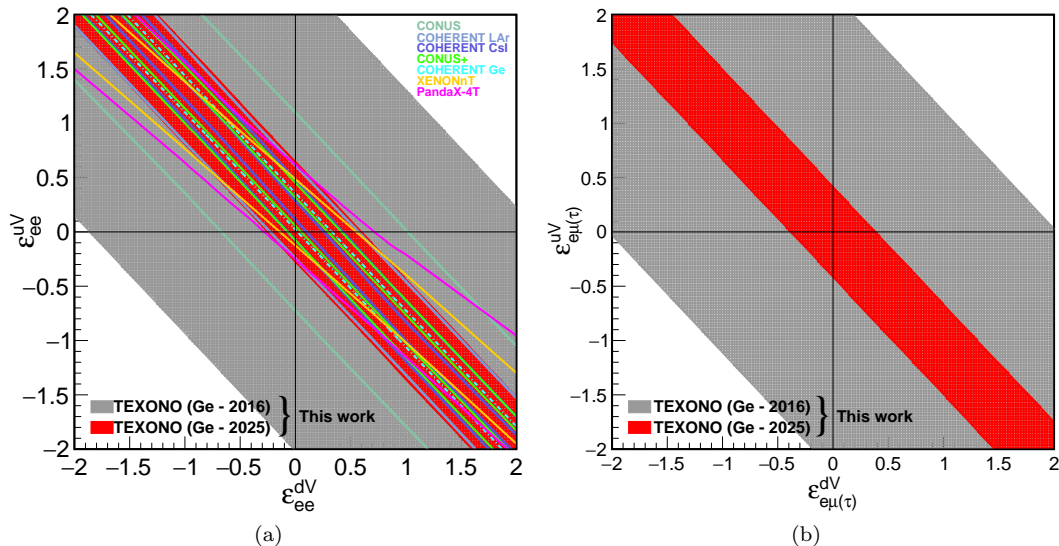


FIG. 8. The 90% CL allowed region for single-type FC-FC and FV-FV parameter spaces for vector-type NSI:  $\epsilon_{ee}^{dV} - \epsilon_{ee}^{uV}$ , and  $\epsilon_{e\mu}^{dV} - \epsilon_{e\mu}^{uV}$ . For comparison, the bounds from other reactor-based experiments (CONUS+ [49], CONUS [57]), accelerator based-experiments (COHERENT CsI and COHERENT LAr [67], COHERENT Ge [74]), as well as dark matter experiments (XENONnT and PandaX-4T) sensitive to CE $\nu$ NS are included [123].

Specifically, the cross-section depends on the condition  $([\epsilon_{ee}^{uV}(2Z + N) + \epsilon_{ee}^{dV}(Z + 2N)] + Q_{SMV})^2 = \text{constant}$ , resulting in two allowed bands with slopes determined by the ratio  $(2Z + N)/(Z + 2N)$  [45, 71]. Even though these degeneracy regions are not visible in current TEXONO data due to the sensitivity limitations, their appearance in other reactor experiments like CONUS+ highlights the potential of reactor experiments to probe such features.

In the case of a single flavor-off-diagonal (FV-FV) parameter spaces, as shown in Fig. 8b, the cross-section takes the form  $\epsilon_{\alpha\beta}^{uV}(2Z + N) + \epsilon_{\alpha\beta}^{dV}(Z + 2N) = \text{constant}$ , with a center at (0,0), and the upper limits form parallel bands. However, unlike the flavor-diagonal FC-FC case in Fig. 8a, in this scenario, with no contribution from SM interference, the band becomes narrower, and results in more stringent bound. Additionally, due to the presence of only a single-type neutrino flux in TEXONO, bounds from  $\epsilon_{e\mu}^{uV} - \epsilon_{e\mu}^{dV}$  and  $\epsilon_{e\tau}^{uV} - \epsilon_{e\tau}^{dV}$  parameter spaces are identical. We represent such cases as  $\epsilon_{e\mu} = \epsilon_{e\tau} \equiv \epsilon_{e\mu(\tau)}$ .

In Fig. 9, we present the 90% CL upper limits for mixed FC-FV and two-type FV-FV parameter spaces. For these scenarios, we explored two different parameter spaces: combinations of  $\epsilon_{\alpha\alpha}^{fV} - \epsilon_{\alpha\beta}^{fV}$ , and  $\epsilon_{\alpha\beta}^{fV} - \epsilon_{ij}^{fV}$ , where  $\alpha, \beta \neq i, j$ . In certain FV cases, where the parameter space involves either two flavor-off-diagonal parameters or a combination of one flavor-diagonal and one flavor-off-diagonal parameter space, the absence of SM interference and the lack of first-order terms of the relevant epsilon parameters in the cross-section, the upper limits cannot be directly set on these parameters. Instead, as shown in Figs. 9a and 9c, the  $\chi^2$  analysis is performed on the epsilon-squared parameters, where  $(\epsilon_{\alpha\beta}^{fV})^2 > 0$ ,

and then subsequently converted into the  $\epsilon_{\alpha\beta}^{fV}$  parameter space. This method allows us to eliminate certain regions of the full elliptical bounds, resulting in semi-elliptical (Fig. 9b) or quarter-elliptical (Fig. 9d) allowed regions. This difference arises because  $\epsilon_{ee}^{fV}$  parameters interfere with the SM and it appears linearly in the cross-section. This linear dependence allows us to place both upper and lower bounds on the parameter. In contrast, for parameters like  $\epsilon_{e\mu}^{fV}$ , which do not interfere with the SM, both terms appear only quadratically in the cross-section. As a result, the sensitivity is limited to the absolute values of the parameters, and only upper limits can be set. Finally, the analyses of other FV parameter spaces in Fig. 9e and 9f follow a similar methodology. To ensure clarity and provide a more concise representation, plots related to the epsilon-squared,  $(\epsilon_{\alpha\beta}^{dV})^2$ , are excluded and only the corresponding  $\epsilon_{\alpha\beta}^{dV}$  parameter spaces are displayed. Also, we adopted existing COHERENT CsI and LAr [67] bounds for  $\epsilon_{ee}^{dV} - \epsilon_{e\mu}^{dV}$  parameter space in Fig. 9e, for comparison.

Figure 10 shows the 90% CL bounds for scalar interactions in all possible FC and FV scenarios. The cross-section for scalar interactions is expressed as a linear combination of the relevant epsilon parameters:  $\epsilon_{\alpha\beta}^{uS}[\mathcal{N}(m_n/m_u)f_{Tu}^n + \mathcal{Z}(m_p/m_u)f_{Tu}^p] + \epsilon_{\alpha\beta}^{dS}[\mathcal{N}(m_n/m_d)f_{Td}^n + \mathcal{Z}(m_p/m_d)f_{Td}^p] = \text{constant}$ , as derived in Eq.(2.28). This linear dependence leads to exclusion bounds in the form of linear bands in the  $\epsilon_{\alpha\beta}^{uS} - \epsilon_{\alpha\beta}^{dS}$  parameter space. The slope of the linear bands is influenced by the relative contributions of the up- and down-quark parameters,  $f_{Tq}^p$  and  $f_{Tq}^n$ , as well as the nuclear masses of the target material. This results in stronger

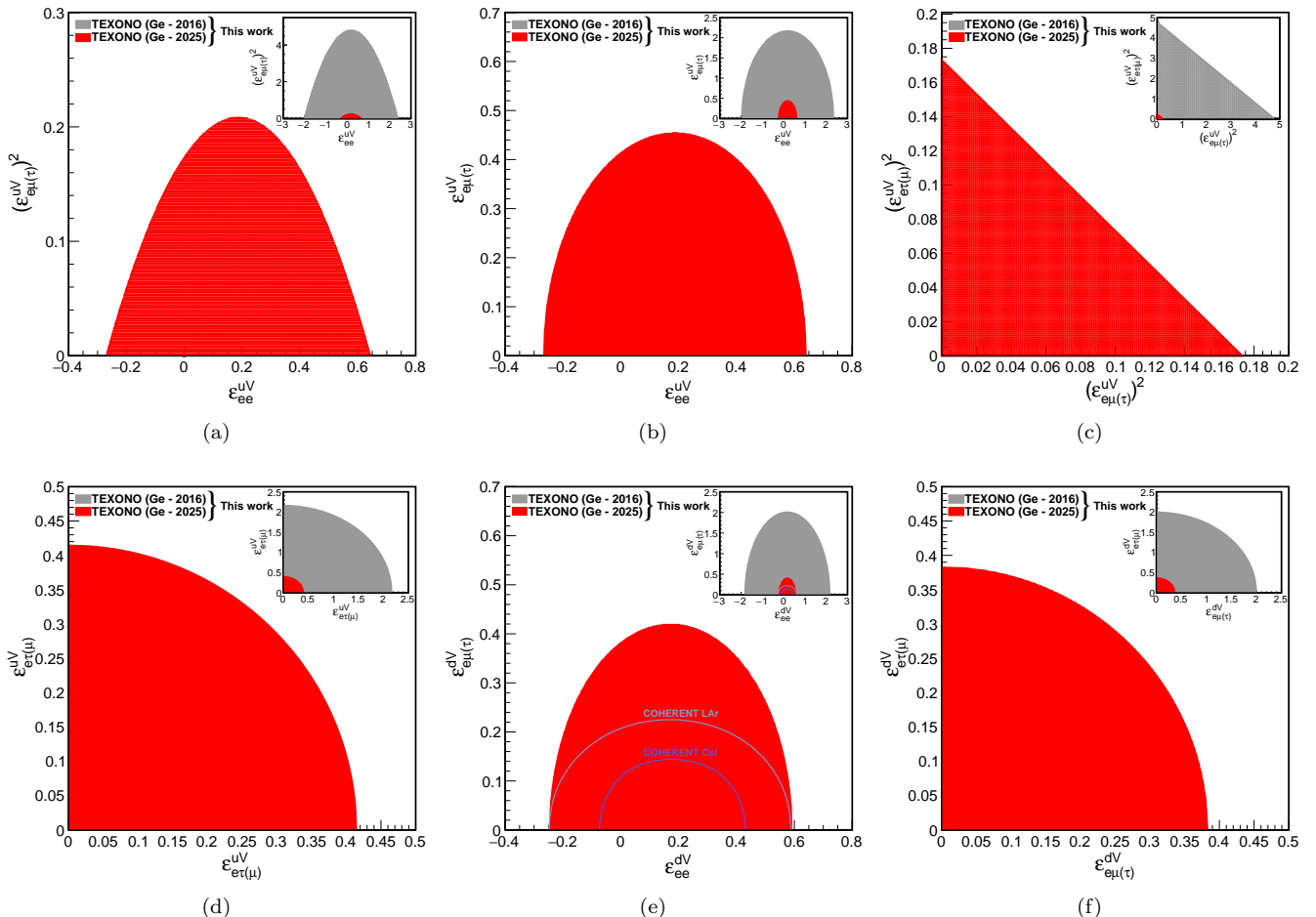


FIG. 9. The 90% CL allowed region for mixed FC-FV and FV-FV parameter spaces for vector-type NSI:  $\epsilon_{ee}^{uV} - (\epsilon_{e\mu(\tau)}^{uV})^2$ ,  $\epsilon_{ee}^{uV} - \epsilon_{e\mu(\tau)}^{uV}$ ,  $(\epsilon_{e\mu(\tau)}^{uV})^2 - (\epsilon_{e\tau(\mu)}^{uV})^2$ ,  $\epsilon_{e\mu(\tau)}^{uV} - \epsilon_{e\tau(\mu)}^{uV}$ ,  $\epsilon_{ee}^{dV} - \epsilon_{e\mu(\tau)}^{dV}$ , and  $\epsilon_{e\mu(\tau)}^{dV} - \epsilon_{e\tau(\mu)}^{dV}$ . For comparison, constraints from COHERENT CsI and COHERENT LAr for the  $\epsilon_{ee}^{dV} - \epsilon_{e\mu(\tau)}^{dV}$  scenario are also superimposed [67].

bounds for heavier nuclei, as larger nuclear masses lead to greater cross-sections. This behavior is evident in Fig. 10b, where we show, for comparison, COHERENT CsI bounds [71] in the  $\epsilon_{e\mu}^{dS} - \epsilon_{e\mu}^{dS}$  parameter space, which appears slightly tighter than TEXONO pPC-Ge.

The bounds shown in Fig. 10c and 10d include parameter spaces for two different FC-FV parameters, resulting in quarter-elliptical regions. To derive these limits, we begin with the epsilon-squared parameter space,  $(\epsilon_{\alpha\beta}^{fS})^2$ , and then transition to the epsilon parameter space,  $\epsilon_{\alpha\beta}^{fS}$ , as explained above. In contrast to the vector case, scalar interactions do not interfere with the SM. This leads to identical bounds in some parameter spaces, thus reducing the number of distinct cases for which independent constraints can be set. For instance, in Fig. 10a, it can be seen that the contributions from the flavor-diagonal  $\epsilon_{ee}^{fS}$  term and the flavor-off-diagonal  $\epsilon_{e\mu(\tau)}^{fS}$  terms yield the same bounds, as both are related to the electron neutrino flux. Similarly, the limits provided by the param-

eter spaces  $\epsilon_{ee}^{fS} - \epsilon_{e\tau(\mu)}^{fS}$  in Figs. 10b and 10c are identical to those in the  $\epsilon_{e\mu(\tau)}^{fS} - \epsilon_{e\tau(\mu)}^{fS}$  parameter spaces. Since these parameter spaces result in the same bounds, only one representative case is shown for clarity.

Following the scalar interaction, we now present a comparative summary of A, T, and P type NSI constraints. Fig. 11 shows the 90% CL upper limits for these three interactions in  $\epsilon_{e\alpha}^{fX} - \epsilon_{e\alpha}^{fX}$  parameter space, where  $X = A, T, \text{ and } P$ . To focus on the most representative and interpretable cases, we omit other parameter combinations. All three interactions produce linear exclusion bands, but with differing slopes due to their distinct dependencies on nuclear recoil energy  $T_N$  and nuclear spin. As described in Eqs. (2.27) and (2.30), both axialvector and tensor interactions are spin-dependent; however, their sensitivities differ depending on how spin-structure functions enter the cross-section. As a result, the axialvector interaction (Fig. 11a) yields comparatively weaker constraints than the tensor interaction (Fig. 11b). In contrast, pseudoscalar interactions in Fig. 11c, while formally spin-

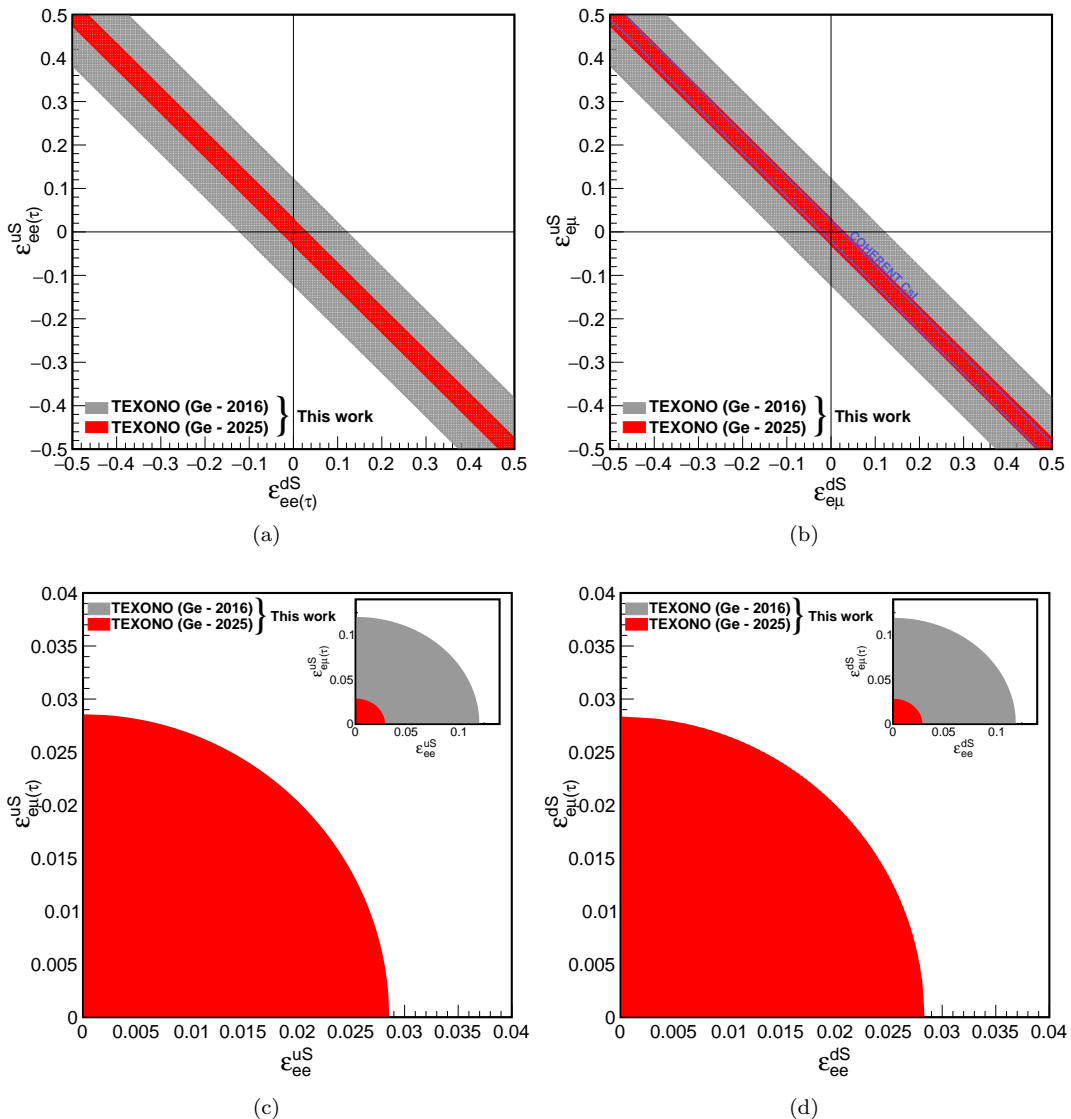


FIG. 10. The 90% CL allowed region for FC and FV parameter spaces for scalar-type NSI:  $\varepsilon_{ee(\tau)}^{dS} - \varepsilon_{ee(\tau)}^{uS}$ ,  $\varepsilon_{e\mu}^{dS} - \varepsilon_{e\mu}^{uS}$ ,  $\varepsilon_{ee}^{uS} - \varepsilon_{e\mu(\tau)}^{uS}$ , and  $\varepsilon_{ee}^{dS} - \varepsilon_{e\mu(\tau)}^{dS}$ . For comparison, the constraint of the  $\varepsilon_{e\mu}^{dS} - \varepsilon_{e\mu}^{uS}$  parameter space from COHERENT CsI is also superimposed [71].

dependent, are highly suppressed by the nuclear recoil energy. As in the simplified model case, this suppression makes the spin contribution negligible, resulting in the weakest bounds among all five type of interactions.

#### D. Bounds from Exotic Neutral-Current Interactions

We now turn to the final aspect of our study, presenting results on exotic neutral current interactions of  $CE\nu$ NS. Based on Eq. (2.34), there are 10 independent parameters dependent on  $C_X$  and  $D_X$ . However, for simplicity, we make choose to set upper limits on the  $\xi_X$  parameters, where  $X = V, A, S,$  and  $T$ . We present our best-

fit measurement results at  $1\sigma$  and upper limits at 90% CL in Table IV, assuming only one-parameter remains while setting others zero for both TEXONO nPC-Ge (2016) and and pPC-Ge (2025) experiments. Similar to the model-independent NSI, the vector term,  $\xi_V$ , in this analysis includes interference with the SM. Additionally, both vector and axialvector terms also exhibit interference. Therefore, when performing a  $\chi^2$ -analysis based on a single-parameter scenario, it is possible to set limits directly on the  $\xi_V$  term. As shown in the first row of Table IV, the bounds at 90% CL are presented as allowed regions rather than upper limits. For the parameters  $\xi_A, \xi_S,$  and  $\xi_T$ , since these parameters appear in the  $\chi^2$  function as the square of the parameters, we turn the parameter-square space into the parameter space, simi-

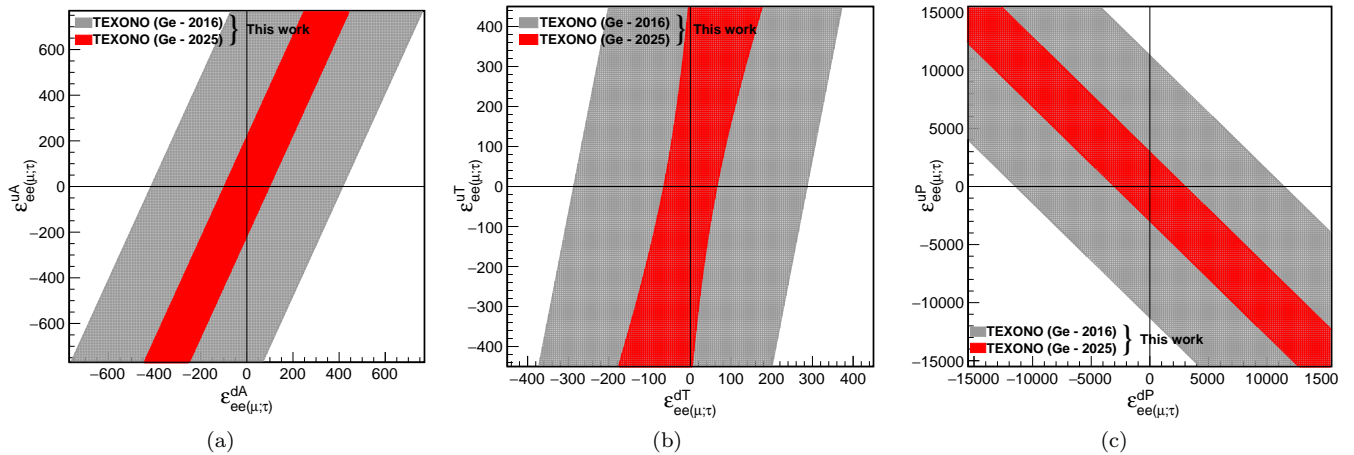


FIG. 11. The 90% CL allowed region for FC-FC parameter spaces for A, P, and T type NSI:  $\epsilon_{ee(\mu;\tau)}^{dA} - \epsilon_{ee(\mu;\tau)}^{uA}$ ,  $\epsilon_{ee(\mu;\tau)}^{dT} - \epsilon_{ee(\mu;\tau)}^{uT}$ , and  $\epsilon_{ee(\mu;\tau)}^{dP} - \epsilon_{ee(\mu;\tau)}^{uP}$ .

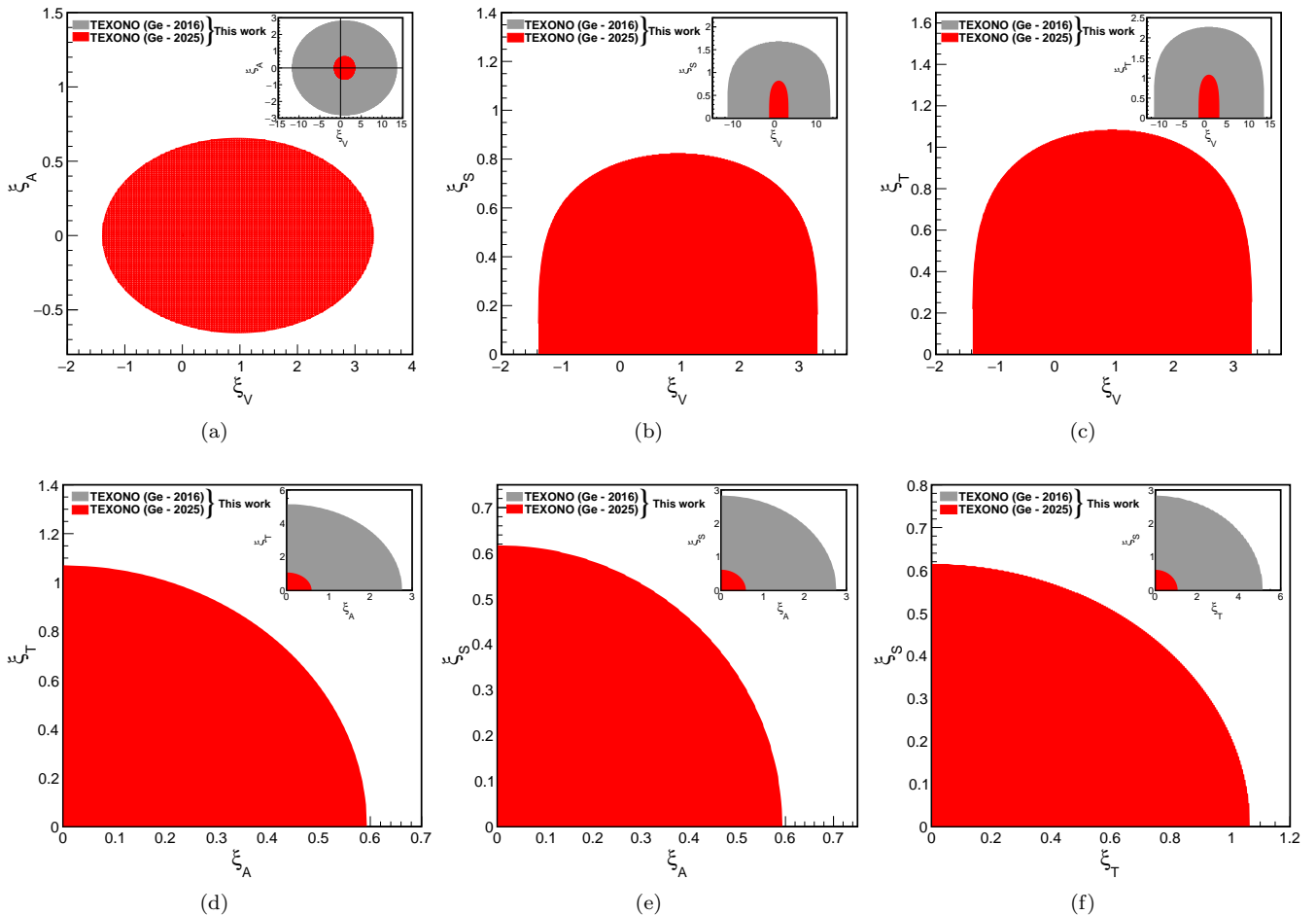


FIG. 12. The 90% CL allowed region of  $\xi_V - \xi_A$ ,  $\xi_V - \xi_S$ ,  $\xi_V - \xi_T$ ,  $\xi_A - \xi_T$ ,  $\xi_A - \xi_S$ , and  $\xi_T - \xi_S$  parameter spaces for exotic neutral current interactions.

lar to the approach used for model-independent NSI. This method allows us to extract upper limits for the param-

eters at 90% C.L.

In Fig. 12, we present the 90% CL upper bounds for

TABLE IV. Summary of the best-fit results and corresponding upper bounds at 90% CL for exotic coupling constant parameters. The results are presented in comparison with two datasets from the TEXONO Collaboration: nPC–Ge (2016) and pPC–Ge (2025). Here only one coupling parameter is assumed to be non-zero for each bound.

Fitting Par	TEXONO nPC–Ge			TEXONO pPC–Ge		
	BFPV $\pm 1\sigma$	90% CL	$\chi^2/\text{dof}$	BFPV $\pm 1\sigma$	90% CL	$\chi^2/\text{dof}$
$\xi_V$	$0.96 \pm 8.04$	$[-9.79, 11.7]$	81.36/120	$0.004^{+2.72}_{-0.79}$	$[-1.147, 3.075]$	87.87/79
$\xi_A^2$	$-0.87 \pm 3.97$	$\xi_A < 2.38$	81.32/120	$0.009 \pm 0.162$	$\xi_A < 0.525$	87.86/79
$\xi_S^2$	$-0.91 \pm 4.18$	$\xi_S < 2.44$	81.32/120	$0.011 \pm 0.175$	$\xi_S < 0.547$	87.86/79
$\xi_T^2$	$-3.06 \pm 13.8$	$\xi_T < 4.44$	81.32/120	$0.024 \pm 0.529$	$\xi_T < 0.946$	87.86/79

the 2-parameter scenario across six possible parameter spaces:  $\xi_V - \xi_A$ ,  $\xi_V - \xi_S$ ,  $\xi_V - \xi_T$ ,  $\xi_A - \xi_T$ ,  $\xi_A - \xi_S$ , and  $\xi_T - \xi_S$ . Unlike the simpler one-parameter case, the two-parameter scenario involves more complex interactions between the parameters, leading to changes in the structure of the allowed regions. The interference between vector term and both the SM and axialvector terms in Eq. (2.34), results in a different analysis procedure for Fig. 12a compared to Figs. 12b and 12c. Similar behavior observed when analysing the vector parameter,  $\xi_V$ , and other parameters,  $\xi_A$ ,  $\xi_S$ , and  $\xi_T$ , in the one-parameter scenario. These interference terms influence how the constraints are applied, which in turn affects the resulting bounds and the shape of the allowed regions in each scenario.

In Fig. 12a, we display the allowed regions for TEXONO pPC–Ge and nPC–Ge in the  $\xi_V - \xi_A$  parameter space, while in Figs. 12b and 12c, we present the corresponding bounds in the  $\xi_V - \xi_S$  and  $\xi_V - \xi_T$  parameter spaces, respectively. Due to the quadratic dependence of  $\xi_S$  and  $\xi_T$  in the cross-section, only the positive regions of these parameters are shown, resulting in semi-elliptical allowed regions, with the  $\xi_V - \xi_S$  parameter space providing more stringent constraints than  $\xi_V - \xi_T$ . In contrast, the  $\xi_V - \xi_A$  parameter space, where both  $\xi_V$  and  $\xi_A$  appear linearly in the cross-section, leads to a symmetric and fully shown parameter space. In the bottom panel of Fig. 12, we present the bounds for the  $\xi_A - \xi_T$ ,  $\xi_A - \xi_S$ , and  $\xi_T - \xi_S$  parameter spaces. Unlike the figures in the upper panel, these scenarios do not include SM interference or mutual interference between the parameters. Since the parameters enters the  $\chi^2$  function in quadratic form, only the positive regions are shown, resulting in quarter-elliptical upper bounds. Notably, TEXONO pPC–Ge exhibits a remarkable improvement over TEXONO nPC–Ge across all exotic neutral current interaction parameter spaces.

### E. Overview of Our Results

In this work, we present a comprehensive analysis of NSI by examining the reactor-based TEXONO CE $\nu$ NS experiment, comparing our results with existing bounds

from both reactor-based and accelerator-based experiments, and highlighting the role of detector advancements in improving parameter constraints. We focus on five different NSI interaction types: vector (V), axialvector (A), scalar (S), pseudoscalar (P) and tensor (T), and present the 90% CL exclusion bounds for key NSI parameters using a 1-bin analysis of the data from TEXONO nPC–Ge(2016) and pPC–Ge(2025).

Besides, one of the key feature of this work is to present the first NSI analysis of TEXONO pPC–Ge (2025) data with a detector threshold of 200 eV. This advancement improves NSI constraints compared to the previous TEXONO nPC–Ge (2016) data and achieves results competitive with other reactor-based experiments. Furthermore, the low-energy nature of reactor neutrinos increases the sensitivity to the NSI model with light mediators, strengthening the constraints, especially in the low momentum transfer regime, where deviations from the SM are more pronounced. Specifically, in certain scenarios, TEXONO experiments yield stronger constraints than accelerator-based results, COHERENT CsI and LAr. For instance, both TEXONO nPC–Ge and pPC–Ge provides more stringent upper limits compared to COHERENT in the light scalar model interaction shown in Fig. 7c. Also, in the light vector mediator case (Fig. 7a) TEXONO pPC–Ge achieves bounds comparable to COHERENT CsI. Moreover, TEXONO pPC–Ge demonstrates a significant improvement over the earlier TEXONO nPC–Ge results and remains competitive with other reactor-based experiments, including CONUS, CONNIE, and Dresden-II (Figs. 7a and 7c). These results highlight the improvements in detector capabilities and its strong potential for investigating NSI.

## V. CONCLUSIONS

Different experimental set-ups with varying detection thresholds and neutrino energy spectra contribute to the exploration of different regions of the NSI parameter space in CE $\nu$ NS. High-energy neutrinos from the SNS are better suited to exploring new physics associated with heavier mediators, while reactor neutrinos emitted at lower energies provide a more powerful search for light

mediators models. This study provides a comprehensive analysis of NSI within the framework of CE $\nu$ NS, utilizing both the simplified model and model-independent approach, as well as exploring exotic neutral interactions, with a particular focus on TEXONO experiment.

We note that the studies of different NSI scenarios have been extensively explored in previous works [45, 46, 48–51, 54–77, 83]. In this study, we present the first dedicated NSI analysis based solely on TEXONO reactor neutrino experiments, using both the nPC–Ge data from 2016 and the recently released pPC–Ge data from 2025. This study provides a systematic assessment of how advances in detector technology have strengthened constraints on NSI parameters and provides new insights into the improving sensitivity of reactor-based CE $\nu$ NS searches. We compare our results with existing bounds in the literature from both accelerator-based experiments, such as COHERENT CsI, LAr, and Ge, and other reactor-based experiments including CONUS+, CONUS, CONNIE, and Dresden-II, as well as the DM experiments like XENONnT, and PandaX-4T.

The abundance of neutrino sources that meet the detection criteria, including terrestrial sources, solar and

atmospheric neutrinos as well as those from accelerators and nuclear power plants, is expected to drive increased scientific activity in the near future. This work underscores the potential for future CE $\nu$ NS experiments to further probe NSI and enhance our understanding of new physics BSM. Moreover, we highlight that future improvements in detector sensitivities could resolve degeneracies and enable tighter constraints, particularly in two-parameter scenarios. Our results may also offer clue for the search for new mediators in the low-energy realm, likely driven by advancements in neutrino or DM experiments.

## ACKNOWLEDGMENTS

This work is supported by the Investigator Award ASIA-106-M02 and Thematic Project AS-TP-112-M01 from the Academia Sinica, Taiwan, and contracts 106-2923-M-001-006-MY5, 107-2119-M-001-028-MY3 and 110-2112-M-001-029-MY3, 113-2112-M-001-053-MY3 from the National Science and Technology Council, Taiwan.

- 
- [1] S. Navas *et al.* [Particle Data Group], “Review of particle physics”, *Phys. Rev. D* **110**, 030001 (2024).
- [2] D. Z. Freedman, “Coherent Neutrino Nucleus Scattering as a Probe of the Weak Neutral Current”, *Phys. Rev. D* **9**, 1389 (1974).
- [3] D. Z. Freedman, D. N. Schramm and D. L. Tubbs, “The Weak Neutral Current and its Effects in Stellar Collapse”, *Ann. Rev. Nucl. Part. Sci.* **27**, 167-207 (1977).
- [4] J. Erler, and M. J. Ramsey-Musolf, “Weak mixing angle at low energies”, *Phys. Rev. D* **72**, 073003 (2005).
- [5] D. Akimov *et al.* [COHERENT Collaboration], “Observation of Coherent Elastic Neutrino-Nucleus Scattering”, *Science* **357**, 6356, 1123 (2017).
- [6] D. Akimov *et al.* [COHERENT Collaboration], “Measurement of the Coherent Elastic Neutrino-Nucleus Scattering Cross Section on CsI by COHERENT”, *Phys. Rev. Lett.* **129**, 8, 081801 (2022).
- [7] D. Akimov *et al.* [COHERENT Collaboration], “First Measurement of Coherent Elastic Neutrino-Nucleus Scattering on Argon”, *Phys. Rev. Lett.* **126**, 1, 012002 (2021).
- [8] S. Adamski *et al.* [COHERENT Collaboration], “First detection of coherent elastic neutrino-nucleus scattering on germanium”, [arXiv:2406.13806 (nucl-ex)].
- [9] D. Akimov *et al.* [COHERENT Collaboration], “The COHERENT Experiment at the Spallation Neutron Source”, arXiv:1509.08702 (2016), and references therein.
- [10] S. J. Brice *et al.*, “A method for measuring coherent elastic neutrino-nucleus scattering at a far off-axis high-energy neutrino beam target”, *Phys. Rev. D* **89**, 072004 (2014).
- [11] H. Bonet *et al.* [CONUS Collaboration], “Constraints on Elastic Neutrino Nucleus Scattering in the Fully Coherent Regime from the CONUS Experiment”, *Phys. Rev. Lett.* **126**, 4, 041804 (2021).
- [12] N. Ackermann *et al.*, “First observation of reactor antineutrinos by coherent scattering”, [arXiv:2501.05206(hep-ex)].
- [13] H. T. Wong, H. B. Li, J. Li, Q. Yue, and Z. Y. Zhou, “Research program towards observation of neutrino-nucleus coherent scattering”, *J. Phys. Conf. Ser.* **39**, 266 (2006).
- [14] A. Aguilar-Arevalo *et al.* [CONNIE Collaboration], “Search for light mediators in the low-energy data of the CONNIE reactor neutrino experiment”, *J. High Energy Phys.* **2020**, 054 (2020).
- [15] J. Billard *et al.*, “Coherent neutrino scattering with low temperature bolometers at Chooz reactor complex”, *J. Phys. G: Nucl. Part. Phys.* **44**, 105101 (2017).
- [16] I. Alekseev *et al.* [ $\nu$ GeN Collaboration], “First results of the  $\nu$ GeN experiment on coherent elastic neutrino-nucleus scattering”, *Phys. Rev. D* **106**, L051101 (2022).
- [17] J. Colaresi, J. I. Collar, T. W. Hossbach, A. R. L. Kavner, C. M. Lewis, A. E. Robinson, and K. M. Yocum “First results from a search for coherent elastic neutrino-nucleus scattering at a reactor site”, *Phys. Rev. D* **104**, 072003 (2021).
- [18] G. Agnolet *et al.* [MINER Collaboration], “Background studies for the MINER Coherent Neutrino Scattering reactor experiment”, *Nucl. Instrum. Meth. A* **853**, 53 (2017).
- [19] R. Strauss, J. Rothe, G. Angloher, *et al.*, “The  $\nu$ -cous experiment: a gram-scale fiducial-volume cryogenic detector for the first detection of coherent neutrino-nucleus scattering”, *Eur. Phys. J. C* **77**, 506 (2017).
- [20] D. Yu. Akimov *et al.*, “The RED-100 experiment”, *JINST* **17** (2022) 11, T11011.

- [21] S. Kerman *et al.*, “Coherency in neutrino-nucleus elastic scattering”, *Phys. Rev. D* **93**, 113006 (2016); V. Sharma *et al.* [TEXONO Collaboration], “Studies of quantum-mechanical coherency effects in neutrino-nucleus elastic scattering”, *Phys. Rev. D* **103**, 9, 092002 (2021).
- [22] E. Aprile *et al.* [XENON Collaboration], “Projected WIMP sensitivity of the XENONnT dark matter experiment”, *JCAP* **11**, 031 (2020).
- [23] J. Aalbers *et al.* [DARWIN Collaboration], “DARWIN: towards the ultimate dark matter detector”, *JCAP* **11**, 017 (2016).
- [24] D. S. Akerib *et al.* [LZ Collaboration], “The LUX-ZEPLIN (LZ) Experiment”, *Nucl. Instrum. Meth. A* **953**, 163047 (2020).
- [25] H. Zhang *et al.* [PandaX Collaboration], “Dark matter direct search sensitivity of the PandaX-4T experiment”, *Sci. China Phys. Mech. Astron.* **62**, 3, 31011 (2019).
- [26] Zihao Bo *et al.* [PandaX Collaboration], “First Indication of Solar  $^8\text{B}$  Neutrinos through Coherent Elastic Neutrino-Nucleus Scattering in PandaX-4T”, *Phys. Rev. Lett.* **133**, 191001 (2024).
- [27] E. Aprile *et al.* [XENON Collaboration], “First Indication of Solar  $^8\text{B}$  Neutrinos via Coherent Elastic Neutrino-Nucleus Scattering with XENONnT”, *Phys. Rev. Lett.* **133**, 191002 (2024).
- [28] P. Vogel and J. Engel, “Neutrino electromagnetic form factors”, *Phys. Rev. D* **39**, 3378 (1989).
- [29] J. Billard, J. Johnston and B. J. Kavanagh, “Prospects for exploring New Physics in Coherent Elastic Neutrino-Nucleus Scattering”, *JCAP* **11**, 016 (2018).
- [30] O. G. Miranda, D. K. Papoulias, O. Sanders, M. Tórtola and J. W. F. Valle, “Future  $\text{CE}\nu\text{NS}$  experiments as probes of lepton unitarity and light-sterile neutrinos”, *Phys. Rev. D* **102**, 113014 (2020).
- [31] M. Cadeddu, C. Giunti, Y. F. Li and Y. Y. Zhang, “Average CsI neutron density distribution from COHERENT data”, *Phys. Rev. Lett.* **120**, 7, 072501 (2018).
- [32] J. R. Wilson, “Coherent Neutrino Scattering and Stellar Collapse”, *Phys. Rev. Lett.* **32**, 849 (1974).
- [33] C. J. Horowitz, K. J. Coakley, and D. N. McKinsey, “Supernova observation via neutrino-nucleus elastic scattering in the CLEAN detector”, *Phys. Rev. D* **68**, 023005 (2003).
- [34] J. Learned, “Reactor Monitoring (near and far) with Neutrinos”, *Nucl. Phys. B, Proc. Suppl.* **143**, 152 (2005).
- [35] K. Patton, J. Engel, G. C. McLaughlin, and N. Schunck, “Neutrino-nucleus coherent scattering as a probe of neutron density distributions”, *Phys. Rev. C* **86**, 024612 (2012).
- [36] V. Brdar, W. Rodejohann and X. J. Xu, “Producing a new Fermion in Coherent Elastic Neutrino-Nucleus Scattering: from Neutrino Mass to Dark Matter”, *J. High Energy Phys.* **2018**, 024 (2018).
- [37] J. Liu, X. Chen and X. Ji, “Current status of direct dark matter detection experiments”, *Nature Phys.* **13**, 3, 212-216 (2017).
- [38] M. Schumann, “Direct Detection of WIMP Dark Matter: Concepts and Status”, *J. Phys. G* **46**, 10, 103003 (2019).
- [39] J. Monroe and P. Fisher, “Neutrino backgrounds to dark matter searches”, *Phys. Rev. D* **76**, 033007 (2007).
- [40] A. Gutlein *et al.*, “Solar and atmospheric neutrinos: Background sources for the direct dark matter searches”, *Astropart. Phys.* **34**, 90 (2010).
- [41] M. Drees and G. Gerbier, “Review of Particle Physics”, *Chin. Phys. C* **38**, 353 (2014), and references therein.
- [42] The DarkSide-20k Collaboration, “DarkSide-20k sensitivity to light dark matter particles”, *Commun. Phys.* **7**, 422 (2024).
- [43] L. M. Krauss, “Low-energy neutrino detection and precision tests of the standard model”, *Phys. Lett. B* **269**, 407-411 (1991).
- [44] K. Scholberg, “Prospects for measuring coherent neutrino-nucleus elastic scattering at a stopped-pion neutrino source”, *Phys. Rev. D* **73**, 033005 (2006).
- [45] J. Barranco, O. G. Miranda, and T. I. Rashba, “Probing new physics with coherent neutrino scattering off nuclei”, *J. High Energy Phys.* **12**, 021 (2005); J. Barranco, O. G. Miranda, and T. I. Rashba, “Sensitivity of low energy neutrino experiments to physics beyond the standard model”, *Phys. Rev. D* **76**, 073008 (2007).
- [46] Y. Farzan, M. Lindner, W. Rodejohann and X. J. Xu, “Probing neutrino coupling to a light scalar with coherent neutrino scattering”, *J. High Energy Phys.* **2018**, 066 (2018).
- [47] Pablo Blanco-Mas *et al.*, “Clarity through the Neutrino Fog: Constraining New Forces in Dark Matter Detectors”, [arXiv:2411.14206 (hep-ph)].
- [48] J. Barranco, A. Bolanos, E. A. Garces, O. G. Miranda and T. I. Rashba, “Tensorial NSI and Unparticle physics in neutrino scattering”, *Int. J. Mod. Phys. A* **27**, 1250147 (2012).
- [49] M. A. Corona, M. Cadeddu, N. Cargioli, F. Dordei, and C. Giunti, “Reactor antineutrinos  $\text{CE}\nu\text{NS}$  on germanium: CONUS+ and TEXONO as a new gateway to SM and BSM physics”, [arXiv:2501.18550(hep-ph)].
- [50] Manfred Lindner, Werner Rodejohann and Xun-Jie Xu, “Coherent neutrino-nucleus scattering and new neutrino interactions”, *J. High Energy Phys.*, **2017**, 97 (2017).
- [51] O. G. Miranda, and H. Nunokawa, “Non standard neutrino interactions: current status and future prospects”, *New J. Phys.* **17**, 095002 (2015).
- [52] A. N. Khan, W. Rodejohann, “New physics from COHERENT data with improved Quenching Factor”, *Phys. Rev. D* **100**, 113003 (2019).
- [53] A. N. Khan, D. W. McKay, W. Rodejohann, “CP-Violating and Charged Current Neutrino Non-standard Interactions in  $\text{CE}\nu\text{NS}$ ”, *Phys. Rev. D* **104**, 015019 (2021).
- [54] M. Alpízar-Venegas, L. J. Flores, Eduardo Peinado, and E. Vázquez-Jáuregui, “Exploring the Standard Model and Beyond from the Evidence of  $\text{CE}\nu\text{NS}$  with Reactor Antineutrinos in CONUS+”, [arXiv:2501.10355 (hep-ph)].
- [55] A. Chattaraj, A. Majumdar, R. Srivastava, “Probing Standard Model and Beyond with Reactor  $\text{CE}\nu\text{NS}$  Data of CONUS+ experiment”, [arXiv:2501.12441 (hep-ph)].
- [56] D. K. Papoulias and T. S. Kosmas, “COHERENT constraints to conventional and exotic neutrino physics”, *Phys. Rev. D* **97**, No.3, 033003 (2018).
- [57] H. Bonet *et al.* [CONUS Collaboration], “Novel constraints on neutrino physics beyond the standard model from the CONUS experiment”, *J. High Energy Phys.* **2022**, 85 (2022).
- [58] A. Aguilar-Arevalo *et al.* [CONNIE Collaboration], “Search for light mediators in the low-energy data of the CONNIE reactor neutrino experiment”, *J. High Energy*

- Phys.* **2020**, 54 (2020).
- [59] O. G. Miranda, D. K. Papoulias, G. S. Garcia, O. Sanders, M. Tortola, and J. W. Valle, “Implications of the first detection of coherent elastic neutrino-nucleus scattering (CEvNS) with Liquid Argon”, *J. High Energy Phys.* **2020**, 130 (2020).
- [60] J. Liao, H. Liu, and D. Marfatia, “Implications of the first evidence for coherent elastic scattering of reactor neutrinos”, *Phys. Rev. D* **106**, 3, L031702 (2022).
- [61] M. A. Corona, M. Cadeddu, N. Cargioli, F. Dordei, C. Giunti, Y. F. Li, E. Picciau, C. A. Ternes, and Y. Y. Zhang, “Probing light mediators and  $(g-2)\mu$  through detection of coherent elastic neutrino nucleus scattering at COHERENT”, *J. High Energy Phys.*, **2022**, 109, (2022).
- [62] P. Coloma, I. Esteban, M. C. Gonzalez-Garcia, L. Larizgoitia, F. Monrabal, and S. Palomares-Ruiz, “Bounds on new physics with data of the Dresden-II reactor experiment and COHERENT”, *J. High Energy Phys.* **2022**, 37 (2022).
- [63] M. Cadeddu, N. Cargioli, F. Dordei, C. Giunti, Y. F. Li, E. Picciau, and Y. Y. Zhang, “Constraints on light vector mediators through coherent elastic neutrino-nucleus scattering data from COHERENT”, *J. High Energy Phys.* **2021**, 116 (2021).
- [64] M. Lindner, T. Rink, and M. Sen, “Light vector bosons and the weak mixing angle in the light of new reactor-based CE  $\nu$  NS experiments”, *J. High Energy Phys.* **2024**, 171 (2024).
- [65] M. Demirci and M. F. Mustamin, “Solar neutrino constraints on light mediators through coherent elastic neutrino-nucleus scattering”, *Phys. Rev. D* **109**, 015021 (2024).
- [66] A. Majumdar, D. K. Papoulias, and R. Srivastava, “Dark matter detectors as a novel probe for light new physics”, *Physical Review D* **106**, 013001 (2022).
- [67] V. De Romeri, O. G. Miranda, D. K. Papoulias, G. Sanchez Garcia, M. Tórtola, and J. W. Valle, “Physics implications of a combined analysis of COHERENT CsI and LAr data”, *J. High Energy Phys.* **2023**, 35 (2023).
- [68] V. De Romeri, D. K. Papoulias, and C. A. Ternes, “Bounds on new neutrino interactions from the first CEvNS data at direct detection experiments”, *arXiv preprint arXiv:2411.11749*
- [69] C. Giunti, “General COHERENT constraints on neutrino nonstandard interactions”, *Phys. Rev. D* **101**, 3, 035039 (2020).
- [70] M. F. Mustamin and M. Demirci, “Study of Non-standard Neutrino Interactions in Future Coherent Elastic Neutrino-Nucleus Scattering Experiments”, *Braz. J. Phys.* **51**, 3, 813-819 (2021).
- [71] S. S. Chatterjee, S. Lavignac, O. G. Miranda, and G. S. Garci, “Exploring the sensitivity to non-standard neutrino interactions of NaI and cryogenic CsI detectors at the Spallation Neutron Source”, *Phys. Rev. D* **110**(9), 095027 (2024).
- [72] S. S. Chatterjee, S. Lavignac, O. G. Miranda, and G. Sanchez Garcia, “Constraining nonstandard interactions with coherent elastic neutrino-nucleus scattering at the European Spallation Source”, *Phys. Rev. D* **107**, 055019 (2023).
- [73] B. C. Canas, E. A. Garces, O. G. Miranda, A. Parada, G. Sanchez Garcia, “Interplay between nonstandard and nuclear constraints in coherent elastic neutrino-nucleus scattering experiments”, *Phys. Rev. D* **101**, 035012 (2020).
- [74] J. Liao, D. Marfatia, and J. Zhang, “Testing for coherence and nonstandard neutrino interactions in COHERENT data”, *Phys. Rev. D* **110**, 055040 (2024).
- [75] D. Aristizabal Sierra, V. De Romeri and N. Rojas, “COHERENT analysis of neutrino generalized interactions”, *Phys. Rev. D* **98**, 075018 (2018).
- [76] L. J. Flores, Newton Nath, and Eduardo Peinado, “CEvNS as a probe of flavored generalized neutrino interactions”, *Phys. Rev. D* **105**, 055010 (2022).
- [77] A. Majumdar, D. K., Papoulias, R. Srivastava, and J. W. F. Valle, “Physics implications of recent Dresden-II reactor data”, *Phys. Rev. D* **106**, 093010.
- [78] R. Abbasi *et al.* [IceCube Collaboration], “All-flavor constraints on nonstandard neutrino interactions and generalized matter potential with three years of IceCube DeepCore data”, *Phys. Rev. D* **104**(7), 072006 (2021).
- [79] A. Kumar *et al.*, “A new approach to probe non-standard interactions in atmospheric neutrino experiments”, *J. High Energy Phys.* **2021**, 159 (2021).
- [80] B. Dev *et al.*, “Neutrino non-standard interactions: A status report”, *SciPost Phys. Proc.* **2**, 001 (2019).
- [81] D. Aristizabal Sierra, N. Rojas and M. H. G. Tytgat, “Neutrino non-standard interactions and dark matter searches with multi-ton scale detectors”, *J. High Energy Phys.* **2018**, 197 (2018).
- [82] J. C. Park, G. Tomar, “Probing Non-Standard Neutrino Interactions with Interference: Insights from Dark Matter and Neutrino Experiments”, *JCAP***08**(2023)025.
- [83] V. D. Romeri, D. K. Papoulias, and G. S. Garcia, “Implications of the first CONUS+ measurement of coherent elastic neutrino-nucleus scattering”, *Phys. Rev. D* **111**,075025.
- [84] I. Bischer and W. Rodejohann, “General neutrino interactions from an effective field theory perspective”, *Nucl. Phys. B* **947**, 114746 (2019).
- [85] C. D. McCoy and M. Massimi, “Simplified models: a different perspective on models as mediators”, *Euro. Jnl. Phil. Sci.* **8**, 99-123 (2018).
- [86] A. K. Soma, M. K. Singh, L. Singh, L. T. Yang, W. Zhao, M. Agartioglu, G. Asryan, Y. Y. Chang, J. H. Chen, Y. C. Chuang, M. Deniz, M. Zeyrek [TEXONO Collaboration], “Characterization and performance of germanium detectors with sub-keV sensitivities for neutrino and dark matter experiments”, *Nucl. Instrum. Methods Phys. Res., Sect. A* **836**, 67 (2016).
- [87] S. Karmakar *et al.* [TEXONO Collaboration], “New Limits on the Coherent Neutrino-Nucleus Elastic Scattering Cross Section at the Kuo-Sheng Reactor-Neutrino Laboratory.”, *Phys. Rev. Lett.* **134**, 121802 (2025).
- [88] N. Fornengo M. Maltoni, R. T. Bayo and J. W. F. Valle, “Probing neutrino nonstandard interactions with atmospheric neutrino data”, *Phys. Rev. D* **65**, 013010 (2001); G. L. Fogli, E. Lisi, A. Mirizzi and D. Montanino, “Re-examining nonstandard interaction effects on supernova neutrino flavor oscillations”, *Phys. Rev. D* **66**, 013009 (2002); A. Esteban-Pretel, R. Tomas and J. W. F. Valle, “Probing nonstandard neutrino interactions with supernova neutrinos”, *Phys. Rev. D* **76**, 053001 (2007).
- [89] O. G. Miranda, M. Maya and R. Huerta, “Update to the neutrino-electron scattering in left-right symmet-

- ric models”, *Phys. Rev. D* **53**, 1719 (1996); J. Barranco, O. G. Miranda and T. I. Rashba, “Sensitivity of low energy neutrino experiments to physics beyond the standard model”, *Phys. Rev. D* **76**, 073008 (2007); A. Bolanos, O. G. Miranda, A. Palazzo, M. A. Tortola, and J. W. F. Valle, “Probing nonstandard neutrino-electron interactions with solar and reactor neutrinos”, *Phys. Rev. D* **79**, 113012 (2009).
- [90] S. Davidson, C. P. na-Garay, N. Rius and A. Santamaria, “Present and future bounds on non-standard neutrino interactions”, *J. High Energy Phys.* **0303**, 011 (2003).
- [91] J. Barranco, O. G. Miranda, C. A. Moura and J. W. F. Valle, “Constraining nonstandard interactions in  $\nu_e e$  or  $\bar{\nu}_e e$  scattering”, *Phys. Rev. D* **73**, 113001 (2006); J. Barranco, O. G. Miranda, C. A. Moura, J. W. F. Valle, “Constraining nonstandard neutrino-electron interactions”, *Phys. Rev. D* **77**, 093014 (2008).
- [92] C. Biggio, M. Blennow and E. Fernandez-Martinez, “General bounds on non-standard neutrino interactions”, *J. High Energy Phys.* **08**, 090 (2009); C. Biggio, M. Blennow and E. Fernandez-Martinez, “Loop bounds on non-standard neutrino interactions”, *J. High Energy Phys.* **03**, 139 (2009).
- [93] M. Deniz *et al.* [TEXONO Collaboration], “Constraints on nonstandard neutrino interactions and unparticle physics with  $\bar{\nu}_e - e^-$  scattering at the Kuo-Sheng nuclear power reactor”, *Phys. Rev. D* **82**, 033004 (2010).
- [94] S. Bilmis, I. Turan, T. M. Aliev, M. Deniz, L. Singh and H. T. Wong, “Constraints on dark photon from neutrino-electron scattering experiments”, *Phys. Rev. D* **92**, 033009 (2015).
- [95] M. Deniz, B. Sevda, S. Kerman, A. Ajjaq, L. Singh, H. T. Wong and M. Zeyrek, “Constraints on scalar-pseudoscalar and tensorial nonstandard interactions and tensorial unparticle couplings from neutrino-electron scattering”, *Phys. Rev. D* **95**, 033008 (2017).
- [96] B. Sevda, A. Sen, M. Demirci, M. Deniz, M. Agartioğlu, A. Ajjaq, S. Kerman, L. Singh, A. Sonay, H. T. Wong and M. Zeyrek, “Constraints on nonstandard intermediate boson exchange models from neutrino-electron scattering”, *Phys. Rev. D* **96**, 035017 (2017).
- [97] M. Deniz *et al.* [TEXONO Collaboration], “Measurement of  $\bar{\nu}_e - e^-$  electron scattering cross section with a CsI(Tl) scintillating crystal array at the Kuo-Sheng nuclear power reactor”, *Phys. Rev. D* **81**, 072001 (2010).
- [98] J. M. Link and X. J. Xu, “Searching for BSM neutrino interactions in dark matter detectors.”, *J. High Energy Phys.* **2019**, 4 (2019).
- [99] P. M. Candela, V. De Romeri, P. Melas, *et al.*, “Up-scattering production of a sterile fermion at DUNE: complementarity with spallation source and direct detection experiments.”, *J. High Energy Phys.* **2024**, 32 (2024).
- [100] M. A. Corona, M. Cadeddu, N. Cargioli, F. Dordei and C. Giunti “Momentum dependent favor radiative corrections to the coherent elastic neutrino-nucleus scattering for the neutrino charge-radius determination”, *J. High Energy Phys.* **2024**, 271 (2024).
- [101] R. H. Helm, “Inelastic and Elastic Scattering of 187-Mev Electrons from Selected Even-Even Nuclei”, *Phys. Rev.* **104**, 1466 (1956).
- [102] G. Duda, A. Kemper and P. Gondolo, “Model Independent Form Factors for Spin Independent Neutralino-Nucleon Scattering from Elastic Electron Scattering Data”, *JCAP* **04**, 012 (2007).
- [103] M. Hoferichter, J. Menéndez, and A. Schwenk, “Coherent elastic neutrino-nucleus scattering: EFT analysis and nuclear responses”, *Physical Review D* **102**, 074018 (2020).
- [104] G. Belanger, F. Boudjema, A. Pukhov, and A. Semenov, “micrOMEGAS3.1 : a program for calculating dark matter observables”, *Computer Physics Communications* **185**, 960 (2014).
- [105] D. G. Cerdeño, M. Fairbairn, T. Jubb, P. A. N. Machado, A. C. Vincent and C. Boehm, “Physics from solar neutrinos in dark matter direct detection experiments”, *J. High Energy Phys.* **2016**, 188 (2016). [erratum: *J. High Energy Phys.* **2016**, 048 (2016)].
- [106] J. Abdallah *et al.*, “Simplified models for dark matter searches at the LHC”, *Phys. Dark Univ.* **9-10**, 8 (2015).
- [107] M. Cirelli *et al.*, “Tools for model-independent bounds in direct dark matter searches.”, *JCAP* **10**(2013)019.
- [108] H. Y., Cheng, & C. W., Chiang, “Revisiting scalar and pseudoscalar couplings with nucleons.”, *J. High Energy Phys.* **2012**, 9 (2012).
- [109] J. B. Dent, B. Dutta, S. Liao, J. L. Newstead, L. E. Strigari and J. W. Walker, “Probing light mediators at ultralow threshold energies with coherent elastic neutrino-nucleus scattering”, *Phys. Rev. D* **96**, 9, 095007 (2017).
- [110] A. Chattaraj, A. Majumdar, D. K. Papoulias and R. Srivastava, “Probing conventional and new physics at the ESS with coherent elastic neutrino-nucleus scattering”, [arXiv:2501.12443v1 (hep-ph) (2025)].
- [111] M. , Hoferichter, *et al.* , “High-precision determination of the pion-nucleon  $\sigma$  term from Roy-Steiner equations.”, *Phys. Rev. Lett.* **115**, 092301.
- [112] R., Gupta, *et al.* , “Flavor diagonal tensor charges of the nucleon from (2+ 1+ 1)-flavor lattice QCD.”, *Phys. Rev. D* **98**, 091501(2018).
- [113] S. Davidson, C. Pena-Garay, N. Rius, and A. Santamaria, “Present and future bounds on non-standard neutrino interactions”, *J. High Energy Phys.*, **03**, 011 (2003).
- [114] Z. Berezhiani, and A. Rossi, “Limits on the non-standard interactions of neutrinos from e+e- colliders”, *Phys. Lett. B*, **535**, 207-218 (2002).
- [115] Y. Farzan, and I. M. Shoemaker, “Lepton flavor violating non-standard interactions via light mediators”, *J. High Energy Phys.*, **2016**, 33 (2016).
- [116] F. T. Avignone and Yu. V. Efremenko, “Neutrino-nucleus cross-section measurements at intense, pulsed spallation sources”, *J. Phys. G: Nucl. Part. Phys.* **29**, 2615 (2003).
- [117] H. T. Wong *et al.*, “Search of neutrino magnetic moments with a high-purity germanium detector at the Kuo-Sheng nuclear power station”, *Phys. Rev. D* **75**, 012001 (2007).
- [118] G. Fernandez Moroni, *et al.*, “Charge coupled devices for detection of coherent neutrino-nucleus scattering.”, *Phys. Rev. D* **91**(7), 072001.
- [119] J. Colaresi, J. I. Collar, T. W. Hossbach, C. M. Lewis, and K. M. Yocum, “Measurement of Coherent Elastic Neutrino-Nucleus Scattering from Reactor Antineutrinos”, *Phys. Rev. Lett.- Supplemental Material* **129**, 211802 (2022).
- [120] J. D. Lewin and P. F. Smith, “Review of mathemat-

- ics, numerical factors, and corrections for dark matter experiments based on elastic nuclear recoil”, *Astropart. Phys.* **6**, 87 (1996).
- [121] A. Bonhomme *et al.*, “Direct measurement of the ionization quenching factor of nuclear recoils in germanium in the keV energy range”, *Eur. Phys. J. C* **82**, 815 (2022).
- [122] Y. Li, G. Herrera and P. Huber, “New Physics versus Quenching Factors in Coherent Neutrino Scattering”, [[arXiv:2502.12308 \(hep-ph\) \(2025\)](#)].
- [123] D. , A. , Sierra, N. , Mishra, and L. , Strigari, “Implications of first neutrino-induced nuclear recoil measurements in direct detection experiments: Probing non-standard interaction via CE $\nu$ NS”, *Phys. Rev. D* **111**, 055007 (2025).